Laboratory Study of Hydrodynamics of Submerged Bridges

by

Maxfield T Dean

Presented to the Faculty of the Graduate School of

The University of Texas at Arlington in Partial Fulfillment

of the Requirements for the Degree of

MASTER OF SCIENCE IN CIVIL ENGINEERING

The University of Texas at Arlington

December 2020

Abstract

Bridges are designed to withstand flood and debris loads; however, it is reported that 53% of bridge failures in the U.S. are caused by hydraulic events, including floods, scour, debris, and drifts. A series of scale flume experiments were conducted to determine flood force effects on bridge superstructures. 1:50 scale models of the Texas Department of Transportation's typical reinforced concrete bridge superstructures were tested. The bridge superstructures included beams (TX28 and TX54 girders, slab beams, and box beams) and an accompanying bridge deck and railing. The drag and lift forces and overturning moments were measured by load sensors for various flow conditions. The experiments were carried out for Froude numbers of 0.2, 0.27, and 0.34 and submergence ratios between 0.25 and 3. The scale model of the superstructure was also tested with debris accumulated on the upstream side of the bridge. Different shapes and amounts of debris were simulated under various flow conditions.

The drag, lift, and moment coefficients were calculated and compared to those in literature. The drag coefficients were found to switch from a decreasing to increasing value around an inundation ratio of 0.8 for all superstructure geometries and follow a third-order polynomial distribution. The lift coefficients also followed a similar third-order polynomial distribution pattern with the inflection point at an inundation ratio of 1.0 for the lower Froude number scenario and 0.8 for the high Froude number scenario. The moment coefficients were found to follow logarithmic distribution patterns and to be affected by bridge deck length and superstructure height. The presence of debris increased the observed drag coefficients for a given Froude number. More studies are required to better understand the interaction between the flood flow and bridge structures at the inundation ratios less than one where the inflection points observed on the drag, lift, and moment coefficient graphs. Also, further study of hydrodynamic forces on scale models of a full-bridge structure, including abutments, pier foundation, pier cap, and bearing, and bridge deck system, is recommended.

Acknowledgments

I would like to thank my colleague Mr. Shah Md Imran Kabir, Ph.D. candidate at the University of Texas at Arlington, who contributed to conducting the laboratory experiments, recording, and processing data, without which these experiments would not be possible.

I wish to acknowledge Mr. Qays Mohammed for his work in modifying the facilities to support the test flume and his material support and expertise, and the machine shop staff of the Department of Mechanical Aerospace Engineering of the University of Arlington, without their exacting work, the scale models could not be built.

I am grateful to the Texas Department of Transportation for providing funding for this project.

And last but not least, Dr. Habib Ahmari, whose guidance, support, and expertise were invaluable and much appreciated.

Table of Contents

List of Tables

List of Figures

List of Symbols

A - area of the submerged object

A_D - projected area of the submerged object upon which the drag force is exerted and normal to the flow

A_L -projected area of the submerged object on which the lift force acts and is parallel to the flow

C_D - drag force coefficient

C_L - lift force coefficient

C_M - overturning moment coefficient

F_B - buoyant force

F_D- drag force, ρ_w= water density at STP

F_L - lift force

g - gravitational acceleration

γ - specific weight (= $\rho_w g$)

h - the depth of water,

h_b - bridge low chord elevation

h_u - upstream water depth

L_m - length of model

L_p - length of the prototype

λ_T - time ratios

λ_V - velocity ratio

M_{corr} - moment correction

M_{CG} - overturning moment force,

M_{PF} - moment generated at the point of fixity or at the pier base

M_{GS} - moment generated at the girder soffit

P_r - proximity ratio

ρ_w - water density at STP

s - superstructure height

T_m- time function of model

T_p - time function of the prototype

V - volume of the bridge elements submerged by the flood water.

v -average stream velocity

V_m - model velocity

V_p - prototype velocity

W - width of the bridge deck

Chapter 1 Introduction

1.1 Background

Bridge design and construction are a significant factor when considering the totality of highway design, safety of transportation, and the streamflow regime and environment. Bridges are designed to withstand flood and debris loads; however, it is reported that 53% of bridge failures in the United States are caused by hydraulic events, including floods, scour, debris, drifts, etc. (Wardhana and Hadipriono, 2003). During high flow events, bridges may become fully or partially submerged, and the flood water exerts significant hydrodynamic forces on the bridges, resulting in shearing and overturning the bridge deck, which may cause bridge failure.

One way to better understand the hydrodynamic interactions that these structures face is by performing physical modeling. While computer simulations can be performed to better replicate field conditions, laboratory testing has its place in isolating variables while providing information to help better calibrate more complex computerized simulations.

1.2 Research Objectives

The overarching objectives of this research were to 1) document the hydrodynamic forces affecting four types of Texas Department of Transportation (TxDOT) highway bridge girder types across a range of submergence scenarios using 1:50 scale physical models in a laboratory test flume and 2) calculate the coefficients of drag, lift, and moment and compare them with previous studies.

1.3 Dissertation Structure

Relevant literature is examined, and the theoretical underpinnings of the experiments are outlined in Chapter 2. These experiments are detailed in Chapter 3, and their results are presented in Chapter 4. The findings of this research are summarized and discussed in Chapter 5, and conclusions and suggestions for future work regarding this topic are presented in Chapter 6.

Chapter 2 Literature Review

River-crossing bridges experience significant forces during flood and storm surges. Accurate estimation of forces exerted by the water flow on bridge superstructures is vital to bridge design and assessment of their vulnerability to floods. The main forces acting on bridge substructures and superstructures (when inundated) are hydrostatic, buoyant, drag, lift, and wave (Arneson, 2013). AASHTO (2012) categorizes flood loads into four categories: static pressure, buoyancy, stream pressure, and wave load. A brief description of the hydrodynamics of bluff bodies and flood forces on inundated bridges is presented below.

2.1 Bluff Body

Bridge superstructures act as a buff body- meaning that when submerged by flowing water, the key drag force is pressure drag and that flow separation occurs over a substantial part of its surface (Jempson, 2000). This flow separation reliably occurs at the upstream surface discontinuities – in the case of these experiments, at the modeled bridge railing and bottom girder edges.

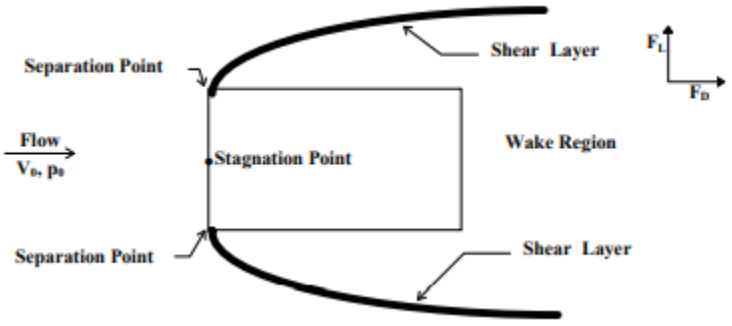

Figure 1- Flow characteristics around a bluff body (Jempson, 2000)

Based on the flow characteristics, the boundary layer around the bluff body can be separated into four different categories, or zones (Naderi, 2018):

- Separation Point – where the boundary layer breaks from the submerged body – in this case, at the sharp corners of the girders and railing,
- Reattachment Point – where the boundary layers re-consolidate with the channel flow

- Stagnation Point – where the maximum pressure occurs, according to Bernoulli's equation; the point where fluid velocity is zero, and
- Wake – low pressure area where the boundary layer separates from the body.

2.2 Flood Forces on Bridge

2.2.1 Buoyancy

Buoyancy is the upward force consequent of the water weight displaced by the submerged portion of the bridge deck structure. It is calculated by using Equation (1):

$$F_B = \rho_w g V \quad (1)$$

where F_B is buoyant force, ρ_w is the density of water, g is the gravitational acceleration, and V is the volume of bridge elements submerged by the flood water.

2.2.2 Hydrostatic Force

Bridges experience hydrostatic forces from upstream and downstream sides due to the water depth, and the net hydrostatic force is a function of differences in the flow depth at both sides of the bridge. American Society of Civil Engineers (ASCE) defines hydrostatic loads as those caused by water either above or below the ground level (Merritt, 1996). The hydrostatic pressure at any point is a function of the depth and density of the fluid. The resultant hydrostatic force can be expressed as:

$$F_R = \frac{1}{2}\gamma h A \quad (2)$$

where γ is a specific weight (= $\rho_w g$), ρ_w is water density, g is gravitational acceleration, h is the depth of water, and A is the projected area of the submerged object.

2.2.3 Drag Force

Drag force is produced by the water current's pressure acting against the submerged bridge deck elements. It has two components: viscous drag and pressure drag. Viscous drag occurs due to tangential shear stress along the surface of the body and depends on the Reynolds number, surface roughness, and the intensity of flow turbulence. Pressure drag is the result of force exerted on the body in the flow direction and is a function of the geometry of the body. The total drag force (F_D)

on a body is obtained by integrating the viscous and pressure drags in the flow direction. The drag force may be estimated as:

$$F_D = \frac{1}{2}\rho_w C_D A_D V^2 \quad (3)$$

where ρ_w is the density of water, C_D is the drag force coefficient, A_D is the projected area of the submerged object upon which the drag force is exerted and normal to the flow, and V is the depth-averaged approach flow velocity. The projected area of the bridge superstructure along the flow direction is calculated as $A_D = s \times L$ where s and L are the bridge thickness (submerged part) and length, respectively.

Drag Coefficient

Derived from the drag force, the drag coefficient C_D, can be defined as:

$$C_D = \frac{2F_D}{\rho_w V^2 A_D} \quad (4)$$

The drag coefficient is a function of the Reynolds number (Re) and Froude number (Fr).

2.2.4 Lift Force

Lift force is the pressure of the water current acting on the submerged portions of the bridge normal to the direction of the flow. It is calculated as:

$$F_L = \frac{1}{2}\,\rho_W\, C_L\, A_L\, V^2 \quad (5)$$

where F_L is the lift force, C_L is the lift force coefficient, ρ_W is the water density, and A_L is the projected area of the submerged object on which the lift force acts and is parallel to the flow. The projected area of the bridge superstructure along the flow direction is calculated as $A_L = W \times L$ where W and L are the bridge width and length, respectively.

Lift Coefficient

The lift coefficient relates the life force exerted on a body to water density, pressure, area, and flow velocity. It allows relative comparisons to be made between different bridge deck types. This coefficient is impacted by the flow conditions characterized by the Reynolds and Froude numbers.

$$C_L = \frac{2\,F_L}{\rho_w V^2 A_L} \quad (6)$$

2.2.5 Overturning Moment

Uneven distribution of forces from the water current acting across the bridge deck cause an overturning moment, which can be estimated with the expression:

$$M_{\mathrm{CG}} = \frac{1}{2} C_{\mathrm{M}}\, \rho_W\, V^2\, W^2 \quad (7)$$

where M_{CG} is the overturning moment force, W is the width of the bridge deck, and C_{M} is the overturning moment coefficient.

Jempson (2000) recommended the following formula for calculating the moment generated from flood and debris acting at a bridge pier's base or point of fixity (Figure 2), allowing for the eccentricity of drag and lift forces.

$$M_{PF} = M_{GS} + F_D \quad (8)$$

where M_{PF} is the moment generated at the point of fixity or at the pier base, M_{GS} is the moment generated at the girder soffit, and F_D is the drag force.

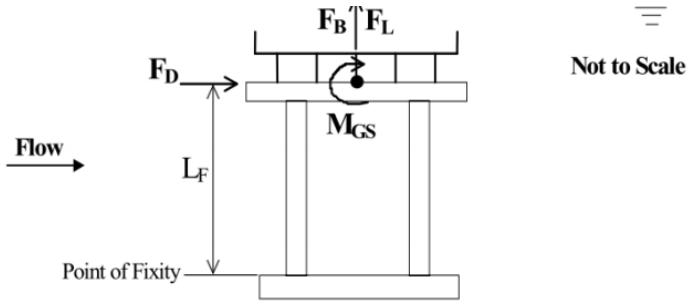

Figure 2- Recommended location of design loads and moment (Jempson, 2000)

Moment Coefficient

The moment coefficient, C_M, is defined as

$$C_M = \frac{2M_{cg}}{\rho_w V^2 L W^2} \quad (9)$$

It is impacted by the Reynolds ad Froude number.

2.2.6 Debris

Debris carried by flood water can hit a bridge with a force that is strong enough to destroy it immediately or make it vulnerable to other causes of failure. Flood debris may include large segments of concrete riverwalks, shipping containers, vehicles, private pontoons, and/or pressure vessels, whereas traditional debris consists of vegetation, trees, mud, soil, sediment, food waste, etc. (Lebbe et al., 2014). Debris may catch and accumulate on the bridge pier, narrowing the waterway opening. The shear impact can cause immediate bridge failure, or the weight of debris, combined with the extreme force of the fast-flowing water, can accelerate the bridge failure. The extent of the damage caused by the impact of the debris depends on the characteristics of the debris and the force of the water flow.

2.3 Definition of Hydrodynamic Parameters in Bridge Studies

The structural responses of bridges under flood loading conditions are highly dependent on the fluid characteristics and configurations of the bridge. The parameters for bridge and flow dimensions are shown below in Figure 3.

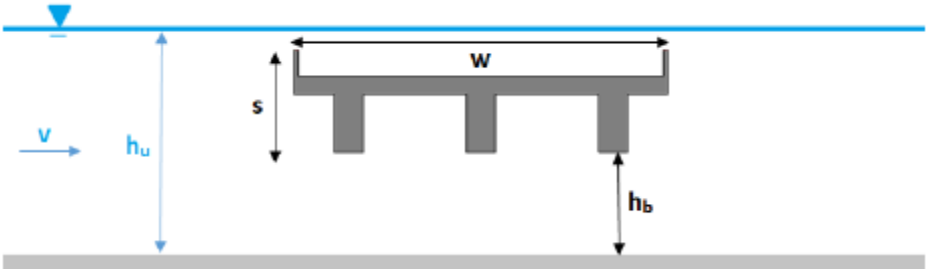

Figure 3- Schematic diagram of a fully submerged bridge deck (Naderi, 2018)

2.3.1 Proximity Ratio

Proximity ratio expresses the relationship between the bridge deck elevation above the channel bottom and the superstructure height.

$$Pr = \frac{h_b}{s} \qquad (10)$$

where Pr is proximity ratio, h_b is bridge low chord elevation, and s is superstructure height.

Jempson (2000) showed that the drag and lift coefficients were affected at higher proximity ratios due to the hydrodynamic interaction between the channel bottom and the bridge superstructure.

2.3.2 Inundation Ratio

The relationship between the superstructure height, elevation above the channel bottom and upstream water depth is known as the inundation ratio, h^*:

$$h^* = \frac{(h_u - h_b)}{s} \quad (11)$$

where h_u is upstream water depth, h_b is bridge low chord elevation, and s is superstructure height.

2.4 Physical Modeling of Hydrodynamic Forces on Bridges

Numerous authors have investigated the hydrodynamic forces that are exerted on partially or fully submerged bridges. Because of the complex behavior of hydrodynamic forces, they are studied by constructing physical models in the laboratory and performing experimental simulations.

A physical model is a reduced-size representation of the prototype (i.e., full-scale structure) that is used during the design stage to optimize a structure and to ensure its safe operation. Physical model studies play an important role in verifying solutions and providing results that cannot be obtained through analytical and numerical solutions. Physical models are commonly used to estimate the hydrodynamic forces on hydraulic structures such as bridges, culverts, spillways, etc. A physical model also helps decision makers visualize the flow field before selecting a suitable design (Chanson, 2004). The following sections discuss the basics of physical modeling and previous physical modeling studies to investigate hydrodynamic forces on bridges.

To test and isolate the hydrodynamic effects of submerged to partially-submerged flow on bridge decks, physical modeling is often conducted in a laboratory setting at a reduced scale from the subjects' prototype.

Jempson (2000) used a 1-m wide test flume to carry out experiments and record the hydrodynamic forces acting on four types of scale model AASHTO bridge superstructures with the option of attaching accompanying piers at a scaled ratio of 1: 25. The effects of the Froude number, degree of submergence (inundation ratio), and proximity of the superstructure to the streambed on the forces and moments acting on the bridge piers and superstructures were investigated. The effects of debris on the forces and bridge stability were also simulated using scaled models of debris mats. Dynamometers and pressure sensors were used to measure the force exerted on the scaled models.

These results provided the base for the design charts in the Australian Bridge Design Standards AS5100 (2004).

The influence of the Froude number on the force coefficients was studied by Malavasi and Guadagnini (2003), who investigated hydrodynamic forces on a fully submerged bridge in a 5-m long, 0.5 m wide, and 0.6 m deep Plexiglas laboratory flume, using the direct force measurement method developed by Cigada et al. (2001). They modeled a cylinder with a rectangular cross section and no piers, with a geometric scale reduction of 1: 33. This simple geometry for the bridge deck was selected to elucidate the mechanisms governing the flow-bridge interaction. They argued that the influence of the flow velocity on the force coefficients is better described by the deck Froude number than by the flow Froude number. Results from the physical modeling showed that the force coefficients are influenced by the inundation ratio (h_*) and the deck Froude number (Fr_D). A value of C_D = 3.4 as an upper limit for the drag force coefficient was reported under flow conditions occurring in natural streams. They found that the presence of the free surface and bottom boundary caused drag and lift forces different from what would be expected from an identical geometry in an unbounded flow situation.

Kerenyi et al. (2009) performed physical modeling of three types of bridge decks to evaluate hydrodynamic forces. The modeling of bridge piers was not included in their study. The experiments were performed in a 12.8 m long, 0.4 m wide, and 0.5 m deep Plexiglas rectangular flume. The reduced scale (1:40) of a six-girder, three-girder, and streamlined bridge deck were tested in the flume. Forces were measured, using a deck force analyzer system. The flow field around the bridges was captured using a PIV (Particle Image Velocimetry) system. Their definition of the drag force distinguished between fully inundated and partially inundated states. The bridge deck experiment results indicated that drag, lift, and moment coefficients had a definite response to the inundation ratio, especially near the partially-inundated to fully inundated transition region. This study also determined that Fr had an influence on the force and moment coefficients, and the bridge type had an influence on drag, lift, and overturning moment coefficients. The forces in the transitional region, where critical lift and moment values occur, were not investigated.

Kara et al. (2015) investigated flow dynamics through a submerged bridge opening with overtopping. The experiment was conducted in a 10-m long, 0.30-m wide tilting flume with a bed slope of 1/2000. The model bridge consisted of a square abutment, with length and width of 0.1 m

and height of 0.05 m; and a rectangular deck, with the thickness of 0.024 m and girder thickness of 0.024 m that extended across the channel. The model bridge was an idealized version of the Towaliga River Bridge near Macon, Georgia. Tests were performed for a variety of water level measurements. From the experiments, it was noted that the overtopping of flow created a horizontal recirculation zone downstream of the abutment, and flow contraction occurred underneath the deck. It was also observed that the overtopping flow reached critical conditions on the deck and created areas of very high turbulence as it plunged in the form of an undular hydraulic jump downstream of the bridge. The location of the highest bed shear stress was found to be underneath the deck, where the flow was contracted and accelerated.

Oudenbroek (2018) conducted a series of experiments in a 4-m long, 0.77-m wide, and 0.5- m high Plexiglas flume. Several bridge decks were modeled at a 1:37 reduced scale. Abutments, piers, and pier foundations were also simulated. Hydrodynamic forces acting on the bridge with and without debris were measured using a 3-dimensional load cell and a torque cell. The effects of flow and debris on drag and lift forces and moment were quantified, and the flow pattern and free surface behavior responsible for the hydrodynamic forces on the bridges were investigated. Unlike previous research, this study assessed the effects of water depth, flow velocity, deck clearance, and blockage ratio on the incipient failure of the bridges. The results of these laboratory experiments showed that the deck-pier system never failed as a unit; piers failed only after deck failure. It was also observed that the presence of debris plays a significant role in the failure of bridges.

2.4.1 Scaling Effects

A physical model used for an experimental study must maintain geometric, kinematic, and dynamic similarities. This ensures that the model replicates the behavior of the prototype when the prototype is subjected to the actual flow.

Geometric Similarity

A model and flow are geometrically similar if the ratio of all of the corresponding dimensions in the model and prototype are equal. The length scaling ratio (λ_L), is calculated as:

$$\lambda_L = \frac{L_m}{L_p} \tag{12}$$

where L_m is the length of model and L_p is the length of the prototype.

Kinematic Similarity

Length and time are the primary dimensions that define kinematic similitude. This similarity ensures that the velocity of the fluid at corresponding points between the model and the prototype has a proportional magnitude and is in the same direction. Since velocity (V) is a function of time (t) and length (L):

$$\lambda_V = \frac{V_m}{V_p} = \frac{L_m}{L_p}\frac{T_p}{T_m} = \lambda_L \lambda_T \quad (13)$$

where λ_V and λ_T are the velocity and time ratios, respectively, V_m= model velocity, V_p = prototype velocity, L_m = length of model and L_p = length of the prototype, T_m = time function of model and T_p = time function of the prototype.

Dynamic Similarity

The dynamic similarity is achieved if the forces acting on the corresponding fluid particles in the model and prototype are proportional:

$$\frac{F_m}{F_i\, m} = \frac{F_p}{F_i\, p} \quad (14)$$

where, $\frac{F_m}{F_i\, m}$ and $\frac{F_p}{F_i\, p}$ are the force ratios in the model and prototype that influence the flow field around the object.

In fluid dynamics, when surface tension and compressibility can be neglected, Reynolds (Re) and Froude (Fr) numbers are the most influential force ratios and should be considered in the design of a physical model. Flow in open channels is governed by inertia force and gravity; therefore, the Froude number can be used to design physical models to study hydrodynamic forces on bridges. The Froude number is calculated as:

$$Fr = \frac{V}{\sqrt{gd}} \quad (15)$$

where V is the flow velocity, d is the flow depth, and g is the acceleration due to gravity

Chapter 3 Experimental Arrangement

3.1 Experimental Flume

The experiments were conducted in the Hydraulics and Fluid Mechanics Laboratory of the University of Texas at Arlington. The experimental flume was an Engineering Laboratory Design Inc. Model B-16 Hydraulic Demonstration Channel plexiglass flume with a 16’ channel length, 12” channel width, and maximum 18” channel depth, as shown in Figure 4. The effective flow capacity of the flume was established to be 410 gpm. The flume was set to have zero longitudinal slope. The adjustable tailgate at the downstream end allowed water elevation to be controlled.

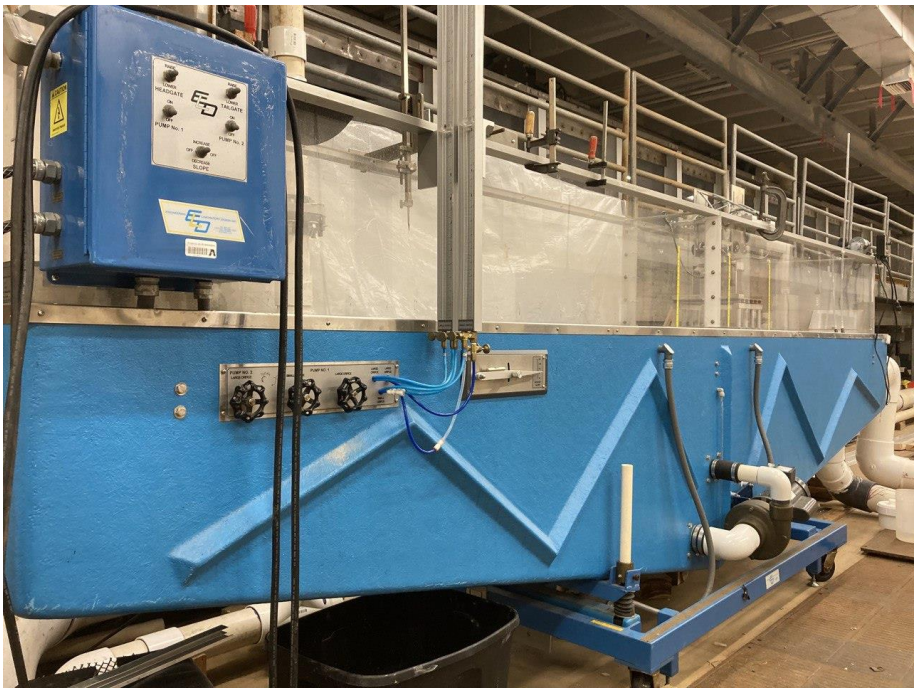

Figure 4- The Model B-16 Hydraulic Demonstration Channel

Initially, the flume was set up with an internally recirculating water supply housed in a fiberglass sump with flow provided by two pumps for a total flow rate of 220 gpm. The stock configuration of the flume provided an insufficient flow rate for Froude numbers over 0.2, so additional modifications were required to allow larger pumps and an external water supply to be used. Two subterrain pumps, each of 220 gpm capacity, were plumbed with 4” inlet line up to the flume inlet.

A six-inch primary and eight-inch overflow outlet were cut into the fiberglass tub to return the additional water input from the subterranean pumps. These outlets were attached to PVC pipes, temporarily preventing the flume's slope from being changed.

The increased flow rate also increased the turbulence of the water. To solve this problem, a three-stage turbulence reduction system was designed from empirical experience. The first stage of the system consisted of a series of rocks placed along the bottom of the flume to reduce the current's entrance velocity (Figure 5). A further set of twin screens served a similar purpose and helped catch debris that entered the system. An adjustable-height wooden float was the final stage of turbulence reduction (Figure 6). Together, these systems helped to minimize surface oscillations, even at high flow rates.

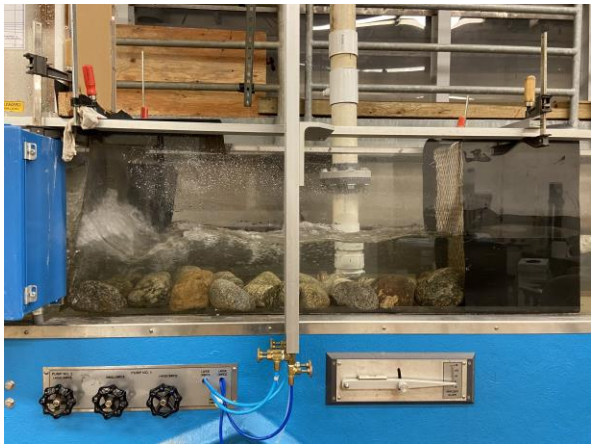

Figure 5- Turbulent reduction system, Stage 1: Rock placement on the flume bottom, and Stage 2: Twin screens

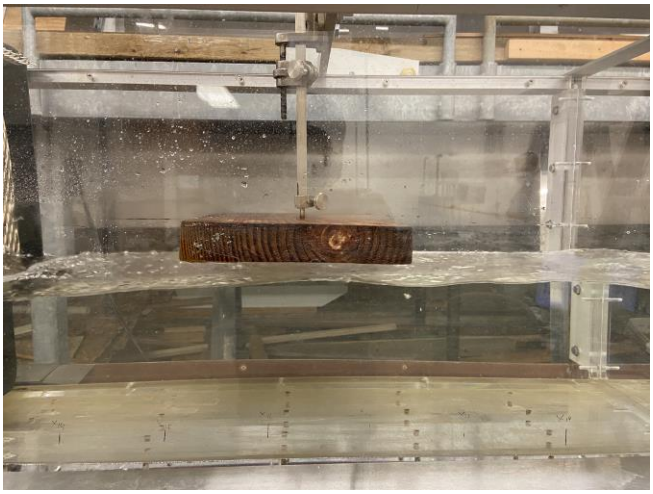

Figure 6- Turbulent reduction system, Stage 3: adjustable-height wooden float

While the fixed area of the flume cross-section causes the average flume velocity to be a function of its flow rate, specific Froude numbers were achieved by controlling the water level and flow rate. To control the water level for a given flow rate, the tailgate was raised or lowered. The flow from the subterranean pumps was controlled both at the pump station itself and adjacent to the flume inlet via a large globe valve.

3.2 Instrumentation

3.2.1 Flow Rate Measurement

The flow rate was measured with a digital SonoTrac ST30 ultrasonic flowmeter attached to the flume's 4" inlet line.

3.2.2 Velocity Measurement

The point velocity upstream of the bridge was taken at the beginning of each experiment using a three-dimensional Acoustic Doppler Velocimeter (ADV). To ensure that it reflected the velocity encountered at the bridge deck, it was recorded downstream of the final flume turbulence reduction feature.

3.2.3 Flow Depth Measurement

Flow depth measurement was recorded using two methods:

- Using a point gauge – its fixed height above the surface of the channel bottom was known, and the flow rate or downstream gate position was manipulated until the water surface just touched the tip of the needle in order to reach the desired depth. This method was useful for verifying that the channel was at a given depth – useful for setting the inundation rate.
- Using measuring tapes fixed to the flume wall, ruled to the nearest 1/32nd inch and usually offset immediately upstream and downstream of the bridge superstructure. They were useful for observing upstream and downstream water level measurements and could be double-checked with the needle method if greater accuracy was desired.

3.2.4 Force and Torque Measurement

The primary instruments used for force and torque measurements included:

- Load Cell – Manufactured by Interface- Model 3A100-100N-D11; 100 N capacity.

- Torque Cell – Manufactured by Interface – Model MRT2 Transducer; 10 NM capacity.

3.2.5 Instrument Frame

An instrument frame was constructed to house the load cell and torque cell and isolate the instruments from external vibrations and keep them well-elevated above the channel water surface due to their vulnerability to submersion.

The initial design called for the moment and load cells to be mounted in parallel and attached to the bridge deck via a single vertical support plate (Figure 7). Vibrations from the pump caused this arrangement to oscillate and negatively impacted the ability of the load cell to register accurate readings. Re-arranging the moment and load cells and thickening the support plate did little to reduce this problem. While adding some transverse stabilizers helped to reduce the z-axis vibrations, they were cumbersome and made bridge elevation changes inconvenient. A better solution was needed.

By doubling the support plates and changing the load cell orientation, the improved instrument frame reduced the oscillations caused by pump vibrations to an acceptable level (Figure 8). Additionally, the two vertical support plates could be adjusted to ensure that the bridge deck was level with the water surface in a parallel and perpendicular manner to the direction of flow (Figures 8 and 9) - an important consideration given the number of submergence ratios studied.

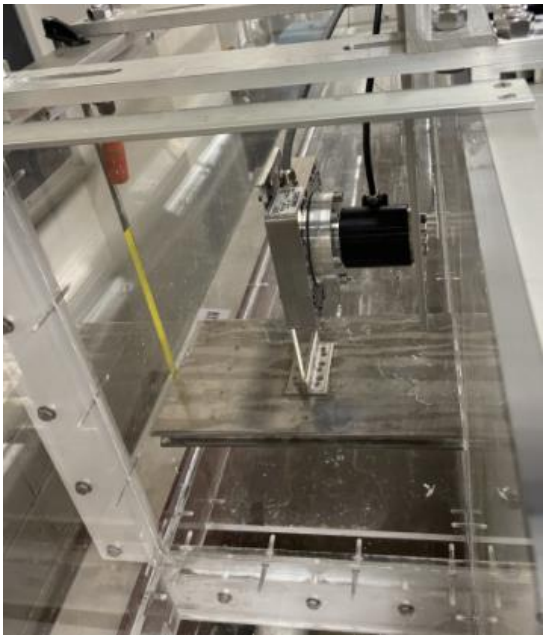

Figure 7- Initial instrument frame arrangement

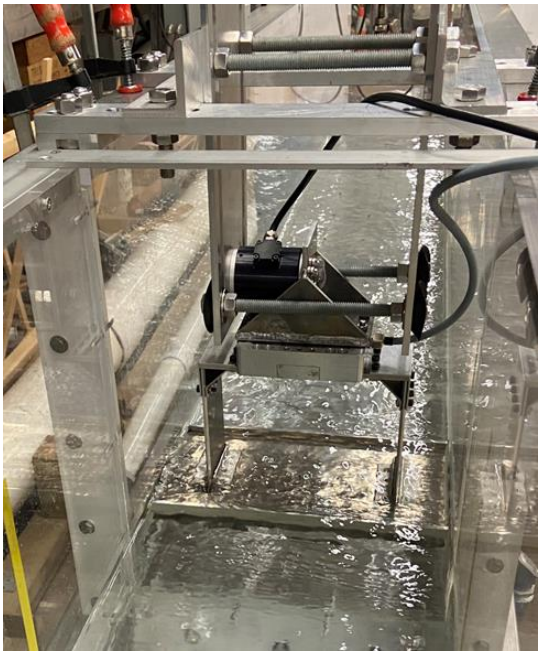

Figure 8- Revised instrument frame

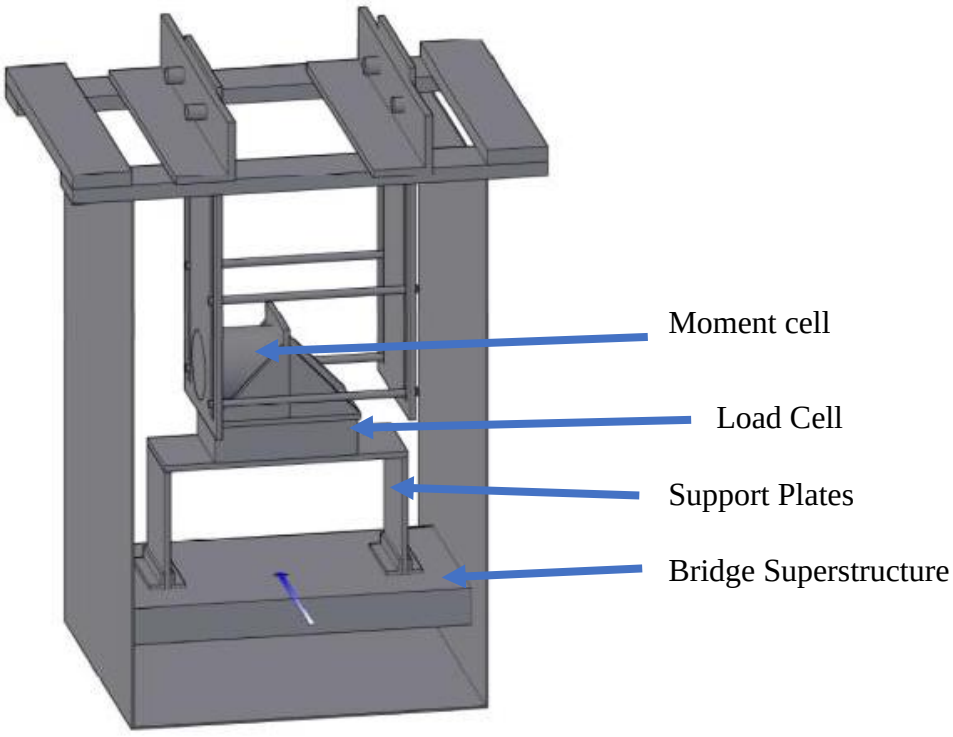

Figure 9- Schematic of the instrument frame used in experiments

3.3 Bridge Deck Models

The scale of the bridge deck test models was primarily constrained by the size of the test flume due to its 12'' width. A 1:50 scale was used since this allowed proximity ratios of up to 3 to be investigated given the 10" water depth at the flume's maximum 440 gpm capacity.

Bridge models consisted of 46' and 26' wide decks with four typical Texas Department of Transportation (TxDOT) beam types:

- TX-28 I Girder – 28" high
- TX-54 I Girder –54" high
- SB-15 Slab Beam – 15" high
- BB-28 Box Beam – 28" high

The decks and girders were machined out of aluminum, a material chosen for its specific weight being similar to the specific weight of reinforced concrete- the material used on the full-size TxDOT bridges.

Railing

Re-bar reinforced railing that is installed on the top of all bridge deck designs as a safety measure. The railing used in the experiment is T221 that measures 32 inches in height, and like the other components, was machined out of aluminum when rendered as a 1:50 model (Figure 10). The bridge deck configurations and components tested are diagramed and described below.

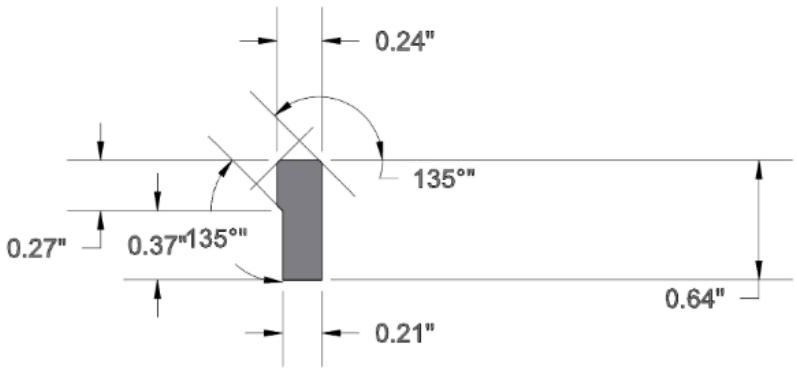

Figure 10- T221 Bridge railing model

3.3.1 Bridge Model 1: TX-28

The Bridge Model 1 consisted of two bridge configurations: 1) a 26’ wide deck with four TX-28 girders and railings (Figure 11), and 2) a 46’ wide deck with six TX-28 girders and railings (Figure 12).

Due to their lower deck height relative to the TX-54, a range of inundation ratios from 0.5 to 2.5 was able to be studied at Froude numbers of 0.2, 0.27, and 0.34, though due to time constraints, only the Fr 0.2 and 0.34 scenarios were tested for the 46’ wide deck. The x, y, z direction forces and moment were recorded at each combination of Froude number and inundation ratio. The model and prototype dimensions are presented in Table 1.

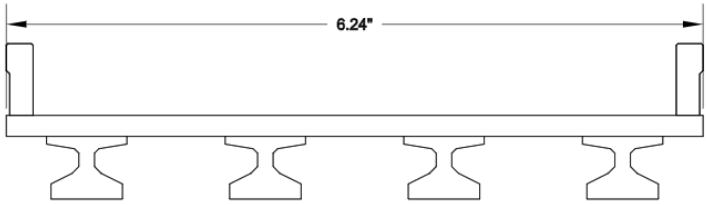

Figure 11- Bridge Model 1: 26’ wide deck with four TX-28 girders

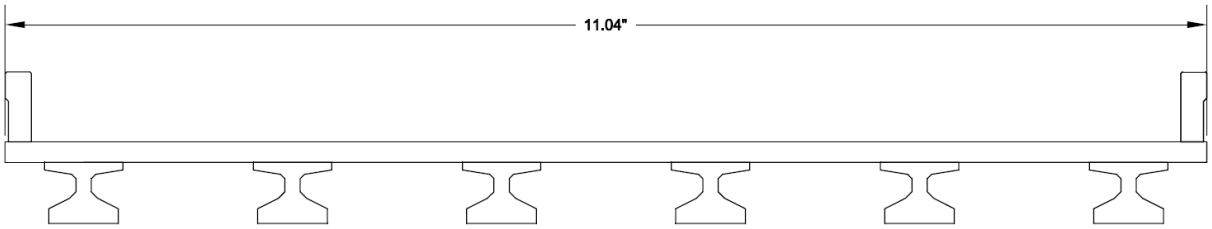

Figure 12- Bridge Model 1: 46’ wide deck with six TX-28 girders

Table 1- Bridge Dimensions (Bridge Model 1: TX-28)

Attribute	**Actual Dimension (in)**	**Scale Dimension (in)**	**Scale Dimension (m)**
Deck thickness (s)	9.375	0.1875	0.0048
Bridge Length (L)	595	11.9	0.302
Width (W)- 26 ft deck	312	6.24	0.16
Width (W)- 46 ft deck	552	11.04	0.280
Girder Height	28	0.56	0.014
Railing height	32	0.64	0.016
Superstructure Height (S)	69.875	1.3875	0.035

3.3.2 Bridge Model 2: TX-54

The Bridge Model 2 consisted of two bridge configurations: 1) a 26’ wide deck with four TX-54 girders and railings (Figure 13), and 2) a 46’ wide deck with six TX-54 girders and railings (Figure 14).

Due to its greater superstructure height relative to the TX-28, a range of inundation ratios from 0.5 to 2.0 were able to be studied at Froude numbers of 0.2, 0.27, and 0.34, though due to time constraints, only the Froude numbers of 0.2 and 0.34 scenarios were tested for the 46’ wide deck. The x, y, z direction load, and moment forces were recorded at each combination of Froude number and inundation ratio. The model and prototype dimensions are presented in Table 2.

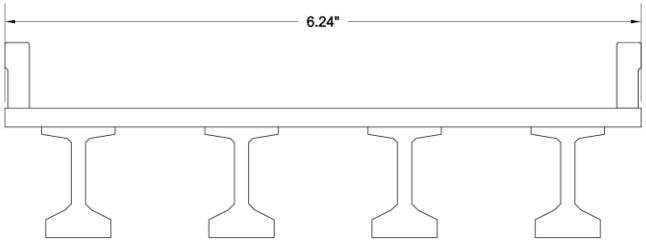

Figure 13- Bridge Model 2: 26’ wide deck with four TX-54 girders

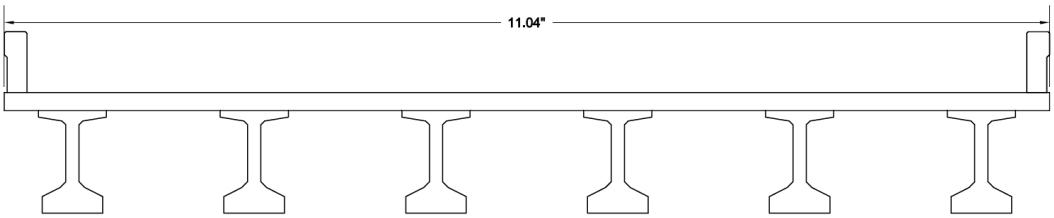

Figure14- Figure 11- Bridge Model 2: 46’ wide deck with six TX-54 girders

Table 2- Bridge Dimensions (Bridge Model 1: TX-54)

Attribute	**Actual Dimension (in)**	**Scale Dimension (in)**	**Scale Dimension (m)**
Deck thickness (s)	9.375	0.1875	0.0048
Bridge Length (L)	595	11.9	0.302
Width (W)- 26 ft deck	312	6.24	0.160
Width (W)- 46 ft deck	552	11.04	0.280
Girder Height	54	1.08	0.027
Railing height	32	0.64	0.016
Superstructure Height (S)	86	1.72	0.043

3.3.3 Bridge Model 3: SB-15 Slab Beam

The Bridge Model 3 consisted of two bridge configurations: 1) a 26’ wide deck with four 5SB-15 slab beams and railings (Figure 15), and 2) a 46’ wide deck with six 5SB-15 and four 4SB-15 slab beams and railings (Figure 16).

Because of its very low superstructure profile (15’’ tall), a range of inundation ratios from 0.5 to 3 was able to be studied at Froude numbers of 0.2, 0.27, and 0.34, though due to time constraints, only the Froude numbers of 0.2 and 0.34 scenarios were tested for the 46’ wide deck. The x, y, z direction load, and moment forces were recorded at each combination of Froude number and inundation ratio. The model and prototype dimensions are presented in Table 3.

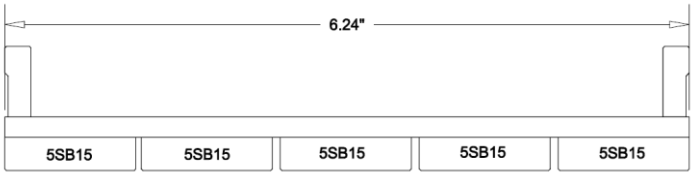

Figure 15- Bridge Model 3: 26’ wide deck with four 5SB-15 slab beams

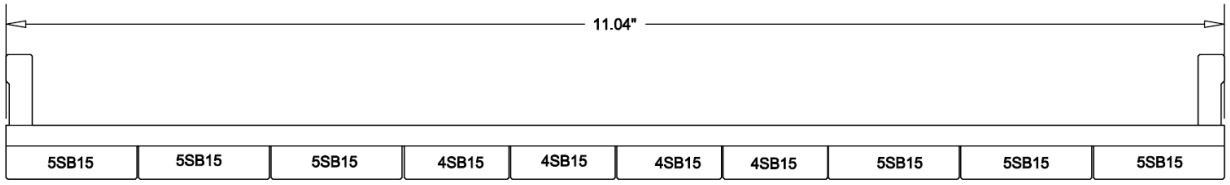

Figure 16- Bridge Model 3: 46’ wide deck with six 5SB-15 and four 4SB-15 slab beams

Table 3- Bridge Dimensions (Bridge Model 3: SB-15 Slab Beam)

Attribute	**Actual Dimension (in)**	**Scale Dimension (in)**	**Scale Dimension (m)**
Deck thickness (s)	9.375	0.1875	0.0048
Bridge Length (L)	595	11.9	0.302
Width (W)- 26 ft deck	312	6.24	0.16
Width (W)- 46 ft deck	552	11.04	0.28
Beam Height	15	0.3	0.0076
Railing height	32	0.64	0.016
Superstructure Height, (S)	40.5	0.81	0.0164

3.3.4 Bridge Model 4: BB-28 Box Beam

The Bridge Model 4 consisted of two bridge configurations: 1) a 26’ wide deck with six BB-28 box beams and railings (Figure 17), and 2) a 46’ wide deck with six 5BB-28 and four 4BB-28 box beams and railings (Figure 18).

Because of its lower superstructure profile, a range of inundation ratios from 0.5 to 2.5 was able to be studied at Froude numbers of 0.2, 0.27, and 0.34, though due to time constraints, only the Froude numbers of 0.2 and 0.34 scenarios were tested for the 46 deck. The x, y, z direction load, and moment forces were recorded at each combination of Froude number and inundation ratio. The model and prototype dimensions are presented in Table 4.

Figure 17- Bridge Model 4: 26’ wide deck with four 5BB-28 box beams

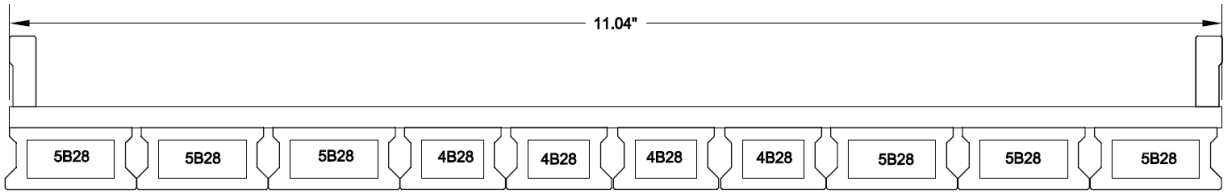

Figure 18- Bridge Model 4: 46’wide deck with six 5BB-28 and four 4BB-28 box beams

Table 4- Bridge Dimensions (Bridge Model 3: BB-28 Box Beam)

Attribute	**Actual Dimension (in)**	**Scale Dimension (in)**	**Scale Dimension (m)**
Deck thickness (s)	9.375	0.1875	0.0048
Bridge Length (L)	595	11.9	0.302
Width (W)- 26 ft deck	312	6.24	0.16
Width (W)- 46 ft deck	552	11.04	0.280
Beam Height	28.1	0.5625	0.0143
Railing height	32	0.64	0.016
Superstructure Height, (S)	60.1	1.205	0.031

3.4 Debris

Three types of debris were tested in the experimental program:

- A flat plate, designed to restrict the flow area past the bridge without increasing the buoyant forces. This scenario is primarily designed to test the effects of flow restriction only (Figure 19).
- A debris mat fixed upstream of the bridge deck, designed to prevent the buoyant nature of the debris mat from acting on the bridge deck. This scenario is designed to better understand how debris with a wedge geometry alters the recorded forces without the buoyant nature of the floating debris coming into play (Figure 20).
- Debris mat attached directly to the bridge deck, allowing buoyant, lift, drag forces to act on the bridge deck – this arrangement is the closest approximation to actual debris conditions. The same debris mat with a wedge geometry used in the fixed upstream scenario was just directly attached to the upstream end of the bridge deck.

3.4.1 Debris Mat Geometry

The flat plate debris section consisted of a 0.12” thick steel plate rigidly fixed to the upstream side of the TX-54- its narrow thickness was intended to minimize buoyant forces while still being thick enough to prevent the current from causing deformation. Its height was set at 2.37”, or 3m high on a 1:50 scale, based on the research of Wellwood & Fenwick (1990), which suggested that 3m is the maximum height of interlocking debris, such as tree limbs, against a bridge superstructure. To ensure an even channel constriction, its width matched the 11.9” width of the bridge deck section.

Based on the work of Jempson (2000), the debris mat was modeled with a flume-width triangular cross-section and its dimensions were fixed at a size of 3 m high (Wellwood & Fenwick, 1990) and 9 m wide, or 2.36” × 7” at a 1:50 scale. The debris mat was made up of an attached collection of buoyant dowels to model the potential moment force that a fixed debris mat might generate on the bridge deck. These 0.75” diameter pinewood dowels, modeled on the average width of trees in the “Southern Forest Region” (Diehl, 1997) that Texas falls into, to better model likely debris conditions, and were fixed together with wood glue.

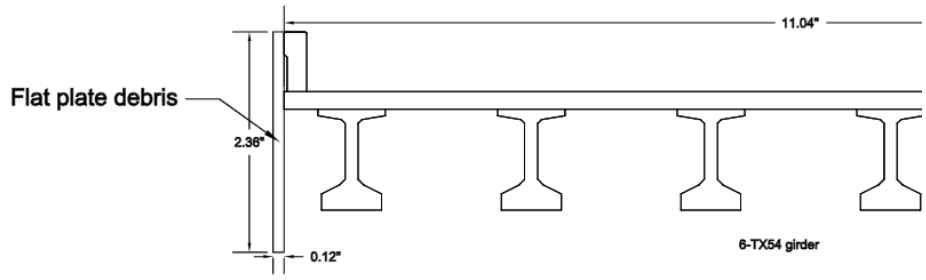

Figure 19a- Geometry of debris flat plate model

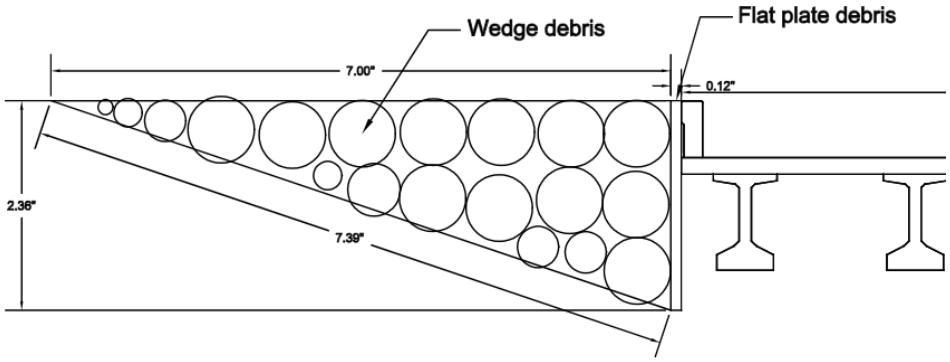

Figure 19b- Geometry of the debris mat model

3.4.2 Debris Test Program

Three experimental arrangements were produced to test the effect that debris produced on the bridge superstructure:

- Debris modeled as a flat steel plate, 2.36” in height and 0.3” in width- this arrangement isolates the drag forces caused by the debris mat while limiting its buoyant and lift effects. The experimental arrangement is shown in Figure 20.

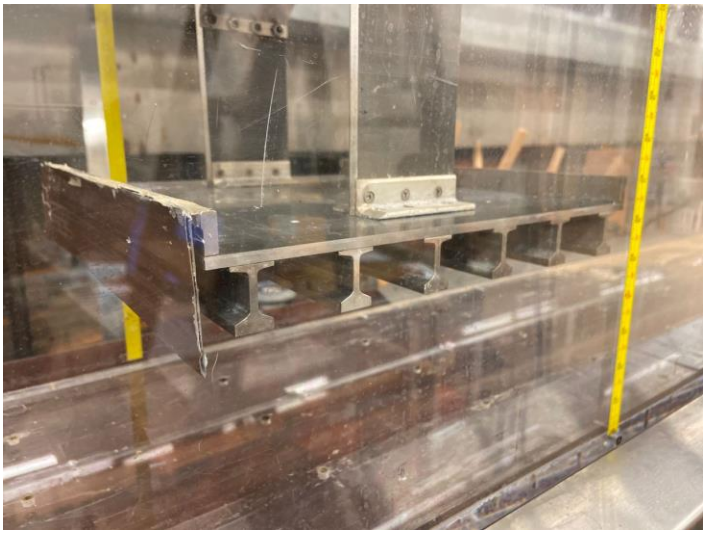

Figure 20- Flat plat debris test arrangement

- Debris mat fixed immediately upstream of the bridge deck- this arrangement allows the drag forces of the debris mat geometry to affect the bridge deck while isolating its buoyant force. The experimental arrangement is shown in Figure 21.
- Debris mat fixed to the bridge deck – this arrangement causes the buoyant moment of the wooden mat to affect the bridge deck. The test arrangement was similar to the previous scenario, as shown in Figure 21 with the exception that the debris wedge was fixed to the bridge deck.

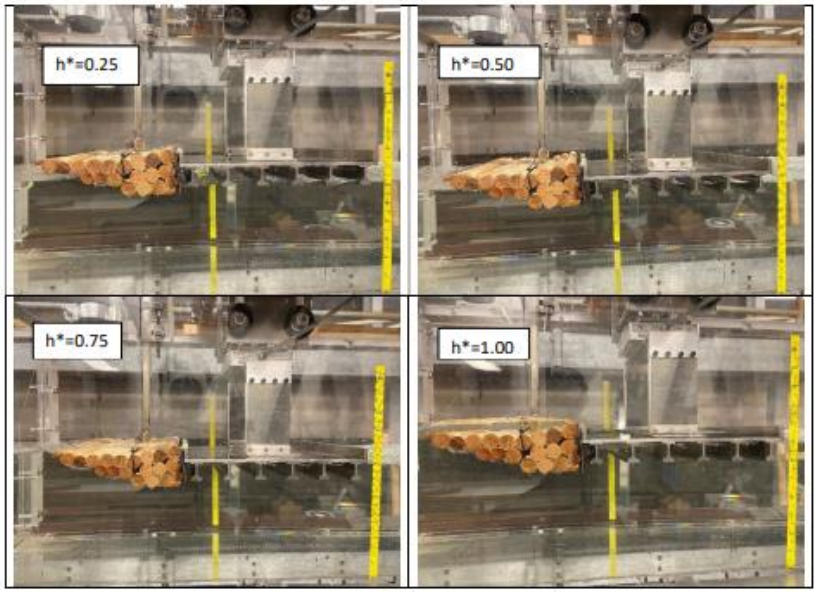

Figure 21- Debris mat debris test arrangement

3.5 Determining Experimental Flow Parameters

3.5.1 Reynolds Number

Since the Reynolds number in these experiments was above 10^4, the relationship between the drag coefficient value and the coefficients on the Reynolds number did not need to be investigated.

3.5.2 Froude Number

The results of the analysis of 598 Texas Department of Transportation administered bridges conducted by Hummel and Pervaiz (2020) showed an average channel Froude number of 0.39 with many bridge channels exceeding that amount- up to 1.3. This is higher than the maximum Froude number of 0.34 that could be simulated in the lab flume due to the limitation of the experimental flume. However, as the results presented in Chapter 4 indicate, this limitation may not be critical, as the trends in coefficient values seem to follow the same patterns, just at lower or higher values. This suggests that these results still offer some value, as they provide a calibration point for the computerized models, which, once calibrated, can then be run at higher Froude numbers.

Chapter 4 Results

The results from the laboratory experiments are presented as the drag, lift, and moment coefficients plots for the wider and narrower bridge deck lengths and for each beam type. The sample calculation of drag, lift, and moment coefficients is presented in Appendix A. A brief commentary will accompany each plot. A plot comparing the drag coefficients for the tested section with and without the debris are presented. The experimental data are compared with Jempson (2000) results for his Type 'A' girder and Type 'B' box superstructures – which can be seen in Figure 22- with the TX 28 and TX54 girders being compared with the Type A superstructure and the slab and box beams being compared with the Type B superstructure. These superstructures had 39' deck width and were tested at 1:25 scale. In contrast, the bridge decks tested during current research experiments had 26' and 46' deck widths and were tested at 1:50 scale.

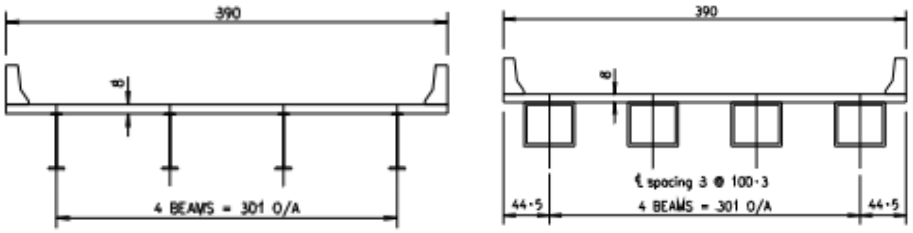

Figure 22- Jempson tested superstructure cross-sections: A-left, and B-right

4.1 Bridge Model 1: TX-28

26-ft Wide Deck

The relationship between the drag coefficient and inundation ratio is presented in Figure 23. The correlation between the average of the drag coefficient data points across all three Froude numbers appears to follow a third-order polynomial pattern, with an average R^2 value of 0.90, though the trend line is only shown for the Fr = 0.34 flow condition. Jempson's results for I-girders appear to show a similar data distribution pattern, though at lower drag coefficient values. One trend across all three sets of Froude numbers is the dip in the drag coefficient between inundation ratios of 0.2 and 0.8, followed by an increase, then a plateau by an inundation ratio of 2.1. This pattern could be due to the interaction between bridge deck's railing and the water surface. As the inundation ratio increases, the action of the water overtopping the upstream railing and turbulently colliding

with the downstream railing could be causing significantly more drag. Once the bridge section is fully submerged, by an inundation ratio of 2.1 for this example, the drag coefficient appears to stabilize.

The relation between the lift coefficient and the inundation ratio is also governed by a third-order polynomial expression as seen in Figure 24. The lift coefficient drops from 0 to -1 at inundation ratio of 1.5 before rising again. Another interesting trend to note is the wider range in the Jempson's lift coefficient value data set relative to this experiment's.

The average of the Froude numbers' moment coefficient's relationship with the inundation ratio can be described with a logarithmic trendline, as seen in Figure 25. The tight grouping of the moment coefficient data relative to the Froude number is also interesting. This seems to imply that the moment coefficient is more heavily impacted by the inundation ratio than the Froude number.

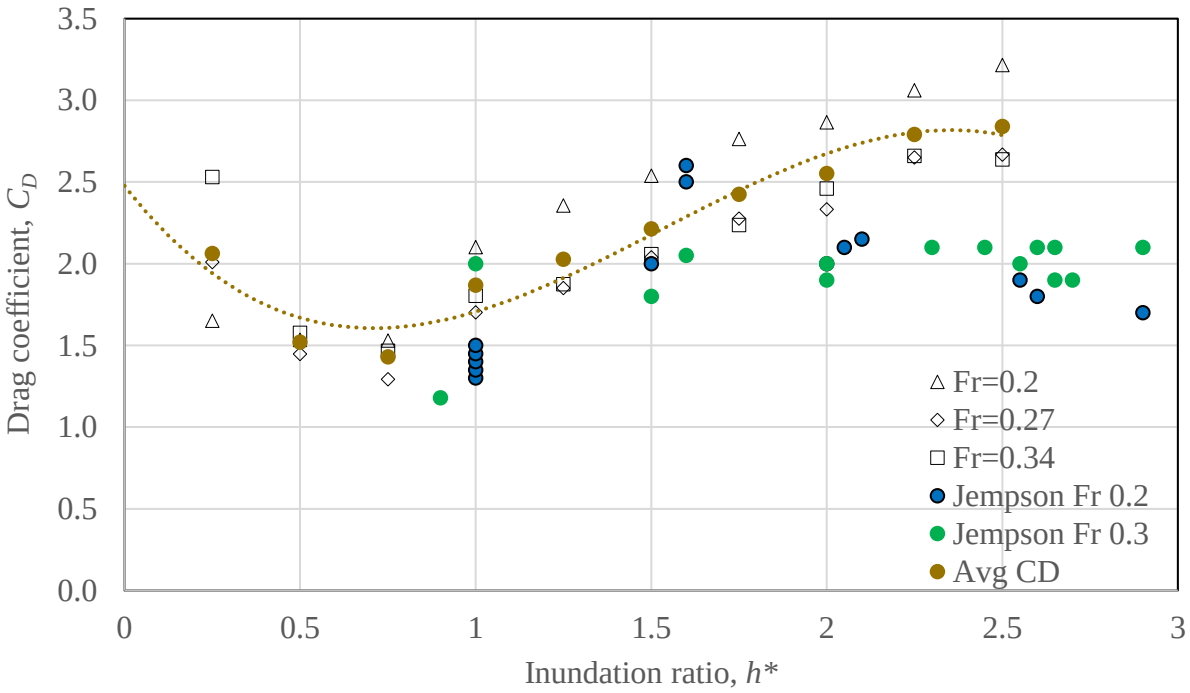

Figure 23- Drag coefficient vs inundation ratio for Bridge Model 1 (TX-28 with 26' wide deck)

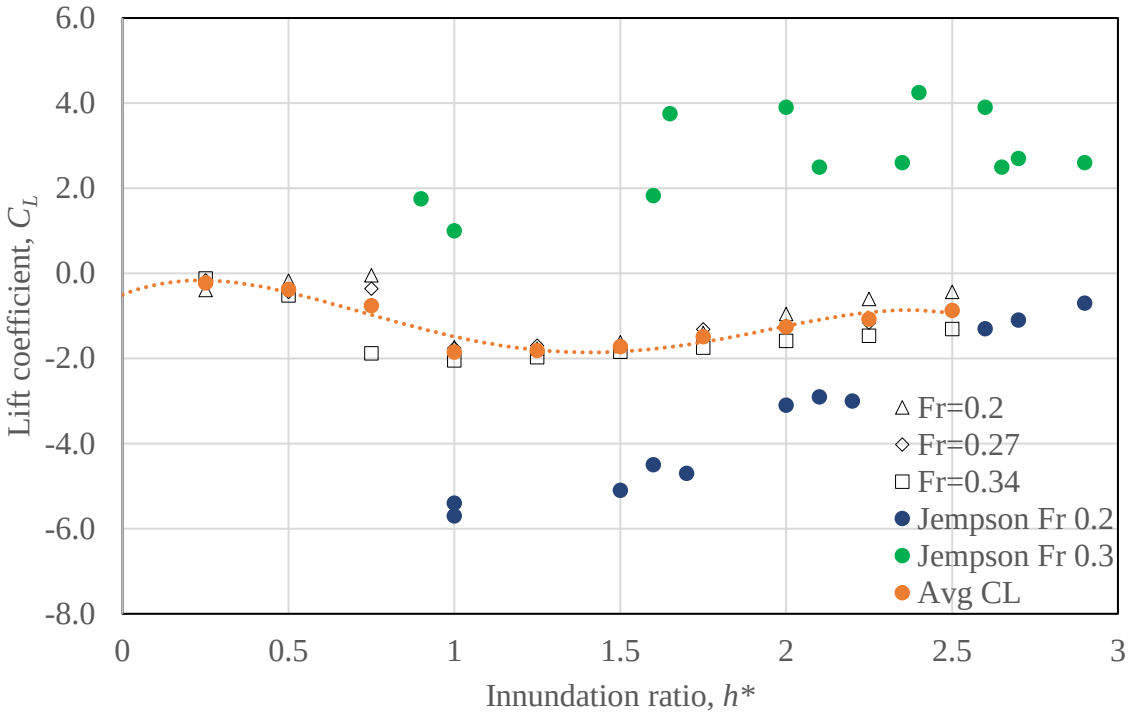

Figure 24- Lift coefficient vs inundation ratio for Bridge Model 1 (TX-28 with 26' wide deck)

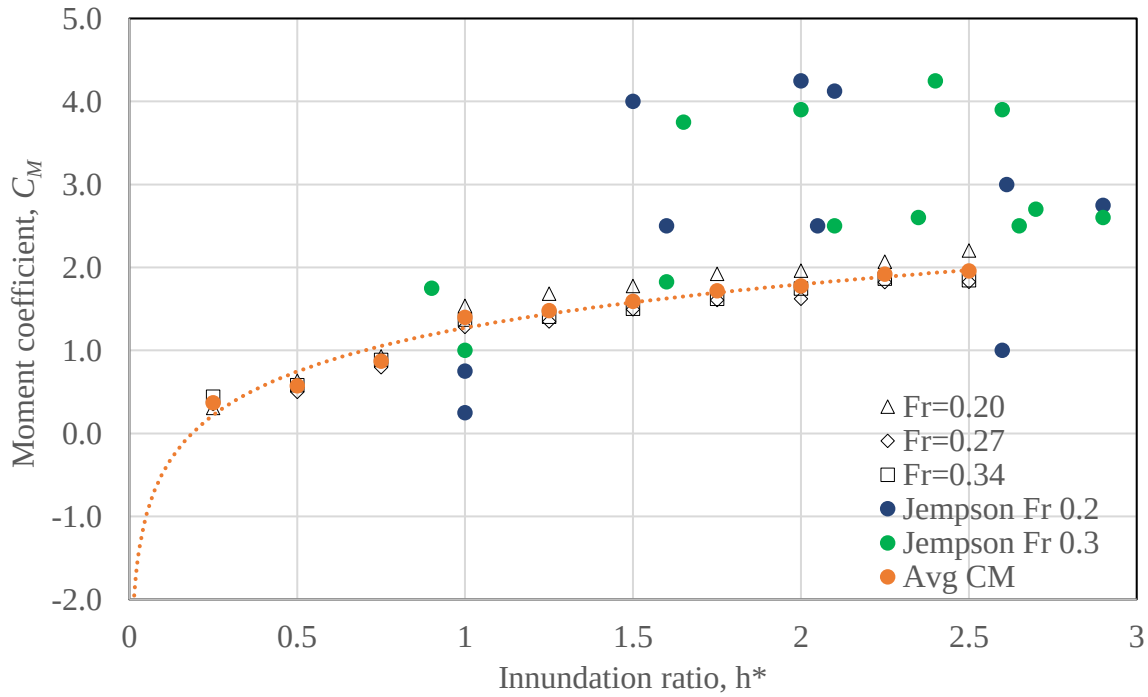

Figure 25- Moment coefficient vs inundation ratio for Bridge Model 1(TX-28 with 26' wide deck)

46-ft Wide Deck

As with the 26 ft deck, the correlation between the average of the drag coefficient data points across all three Froude numbers appears to follow a third-order polynomial pattern, with an R^2 value of 0.90 (Figure 26). Jempson's studies with girders appear to show a similar data distribution pattern, though at lower drag coefficient values. One trend across all both sets of Froude numbers is the dip in drag coefficient between inundation ratios of 0.2 and 0.8, followed by an increase in drag coefficient value. The drag and moment coefficient data (Figures 27 and 28) followed trends similar to the 26-foot-wide deck results.

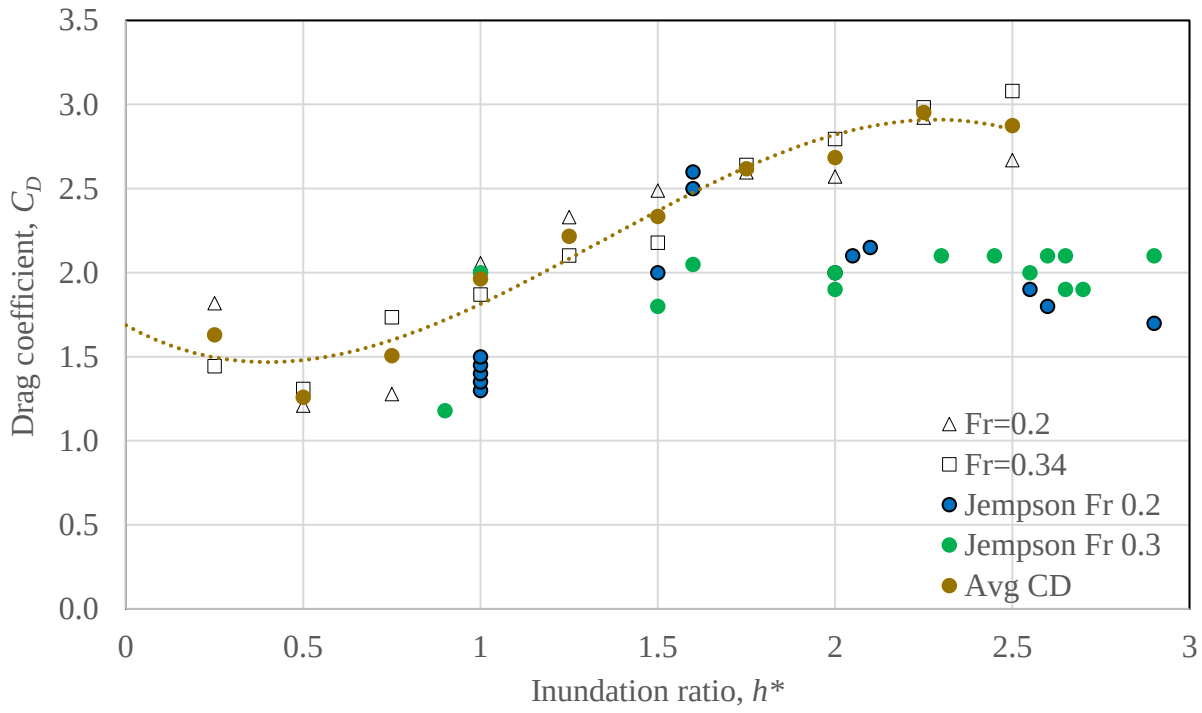

Figure 26- Drag coefficient vs inundation ratio for Bridge Model 1(TX-28 with 46' wide deck)

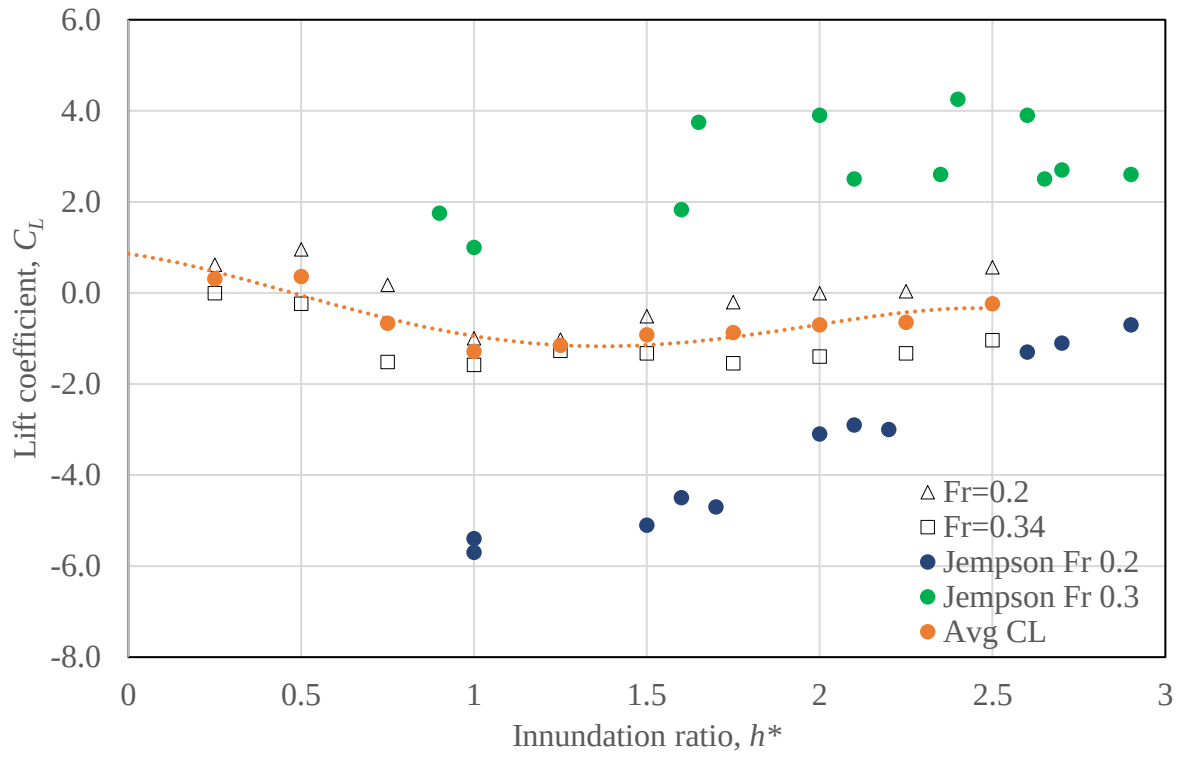

Figure 27- Lift coefficient vs inundation ratio for Bridge Model 1 (TX-28 with 46' wide deck)

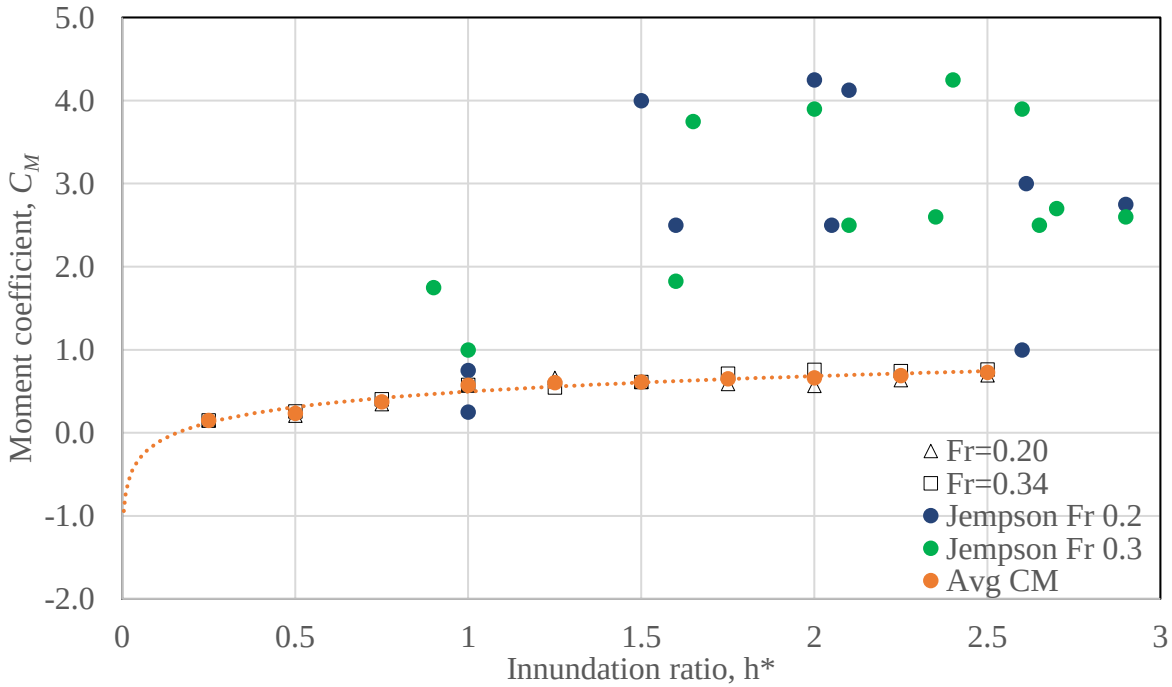

Figure 28- Moment coefficient vs inundation ratio for Bridge Model 1 (TX-28 with 46' wide deck)

4.2 Bridge Model 2: TX-54

26-ft Wide Deck

The relationship between the drag coefficient and inundation ratio is presented in Figure 29. The trend in variation of drag coefficient with inundation ratio and Fr number is similar to those observed in Model 1 with TX-28.

The lift coefficient pattern is harder to discern (Figure 30). It drops until an inundation ratio of 1.0, then increases again until the highest tested inundation ratio of 2. Since the inundation ratio of 1 occurs when the water surface is at the bridge deck elevation, this increase makes intuitive sense: as the amount of water sitting above the bridge deck increases, the net lift forces acting on its bottom surface will also decrease as well. Jempson's data was taken across a wider range of inundation ratios and suggests that had the test flume been large enough to perform deeper inundation ratio tests, the lift coefficient may continue increasing beyond a inundation ratio of 2, which makes sense given that additional water weight would be acting on the bridge deck's surface.

Another point, evident across this data set, as well as Jempson's is the large amount of lift coefficient variability between similar inundation ratio data points.

As seen in Figure 31, the moment coefficient increases with the inundation ratio with a roughly second-order polynomial relationship. The greater the force acting on the bridge through its inundated cross-section, the greater the resultant moment coefficient. The Jempson's data plateaus after a submergence ratio of 3, suggesting that this experimental arrangement might behave similarly, as the two data sets roughly track each other leading up to that point.

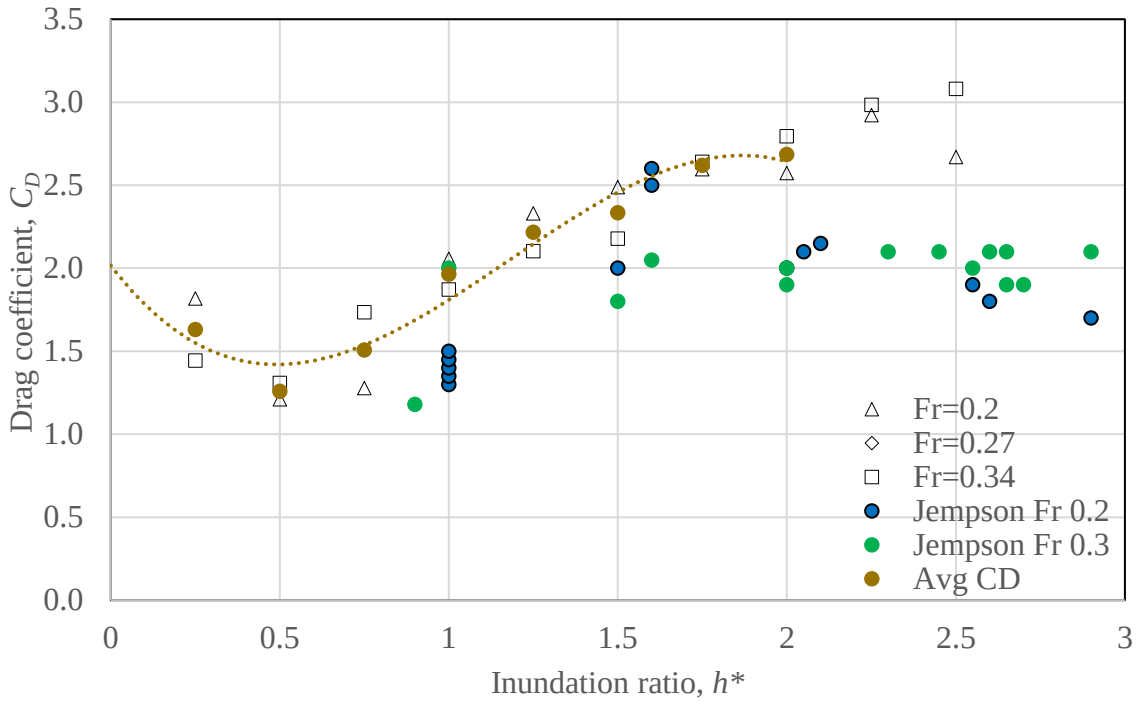

Figure 29- Drag coefficient vs inundation ratio for Bridge Model 2 (TX-54 with 26' wide deck)

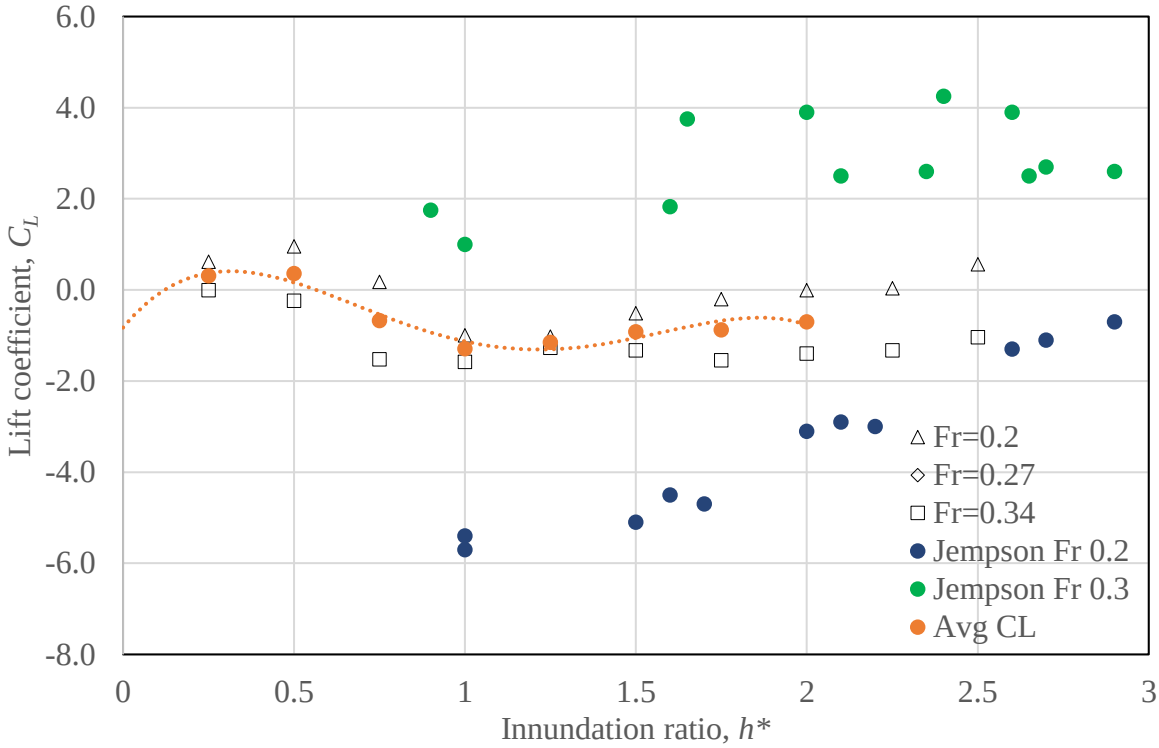

Figure 30- Lift coefficient vs inundation ratio for Bridge Model 2 (TX-54 with 26' wide deck)

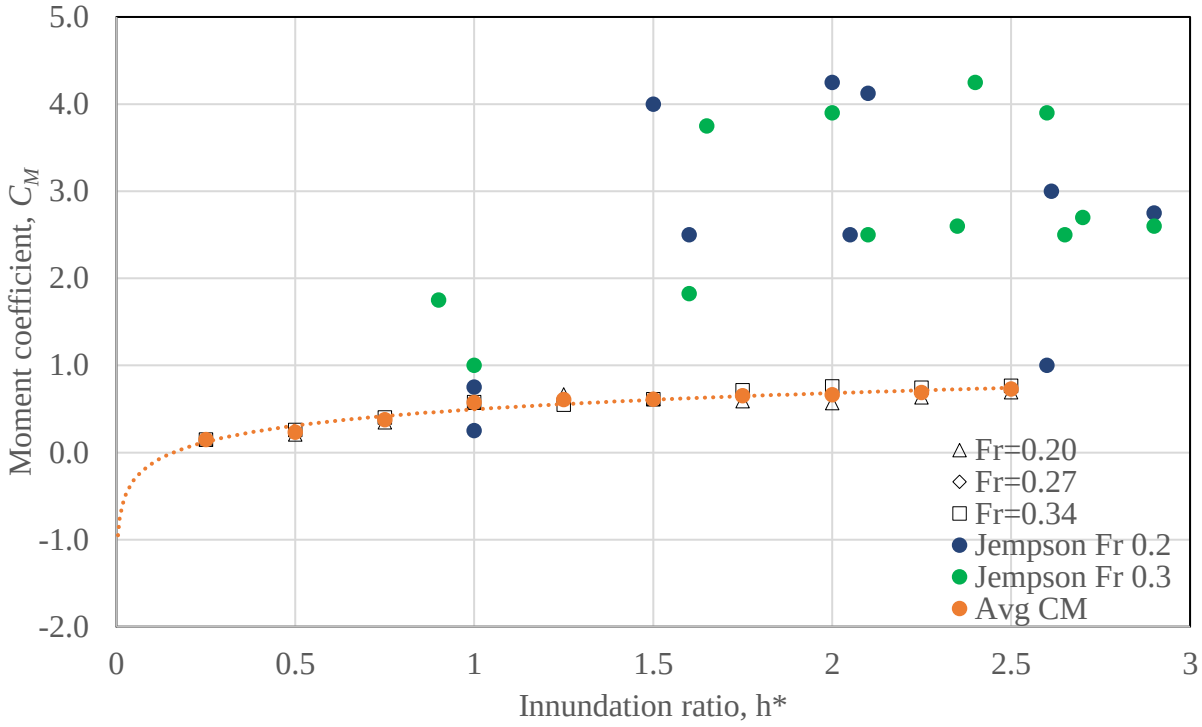

Figure 31- Moment coefficient vs inundation ratio for Bridge Model 2(TX-54 with 26' wide deck)

46-ft Wide Deck

In Figure 32, a third-order polynomial relationship between the inundation ratio and average of the Froude numbers' drag coefficient data can be observed for the wider deck. The drag coefficient decreases from a high of about 2.7 to a low of 1.6 at an inundation ratio of 0.7, and then increases again. This increasing pattern also occurs in the Jempson data set, though Jempson did not test inundation ratios below 0.8, so no direct comparison with the initial drag coefficient drop observed in the data set can be made.

The dip in lift coefficient (Figure 33) in the data begins at an inundation ratio of 1 – this trend can also be observed with a greater magnitude, in the Jempson's data set.

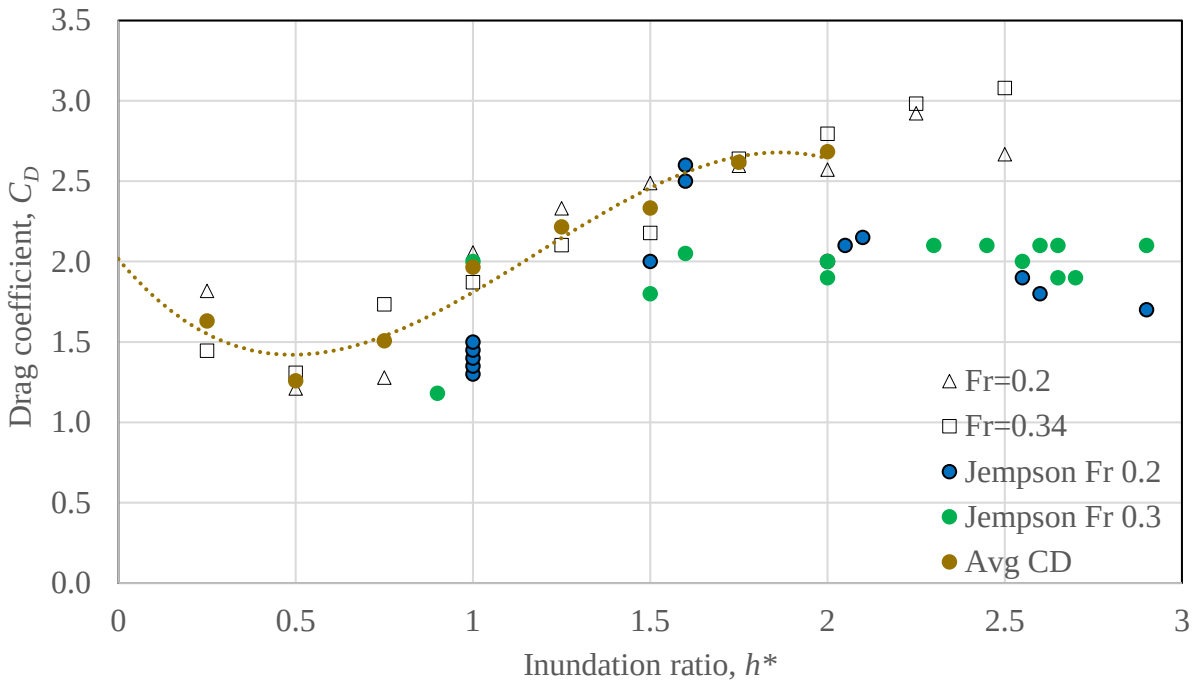

Figure 32- Drag coefficient vs inundation ratio for Bridge Model 2 (TX-54 with 46' wide deck)

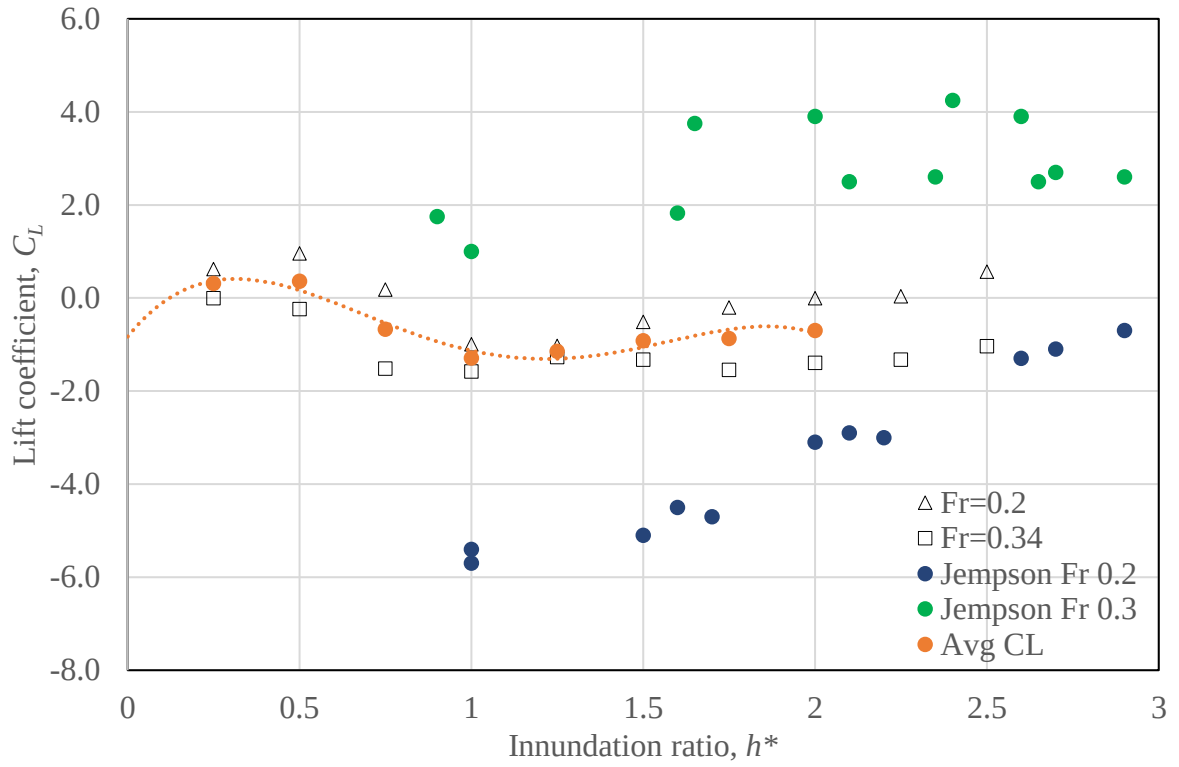

Figure 33- Lift coefficient vs inundation ratio for Bridge Model 2 (TX-54 with 46' wide deck)

In Figure 34, the moment coefficient clearly increases as the inundation ratio increases- a similar, albeit steeper, increase is also observable in the Jempson data set. The greater the force acting on the bridge through its inundated cross-section, the greater the resultant moment coefficient.

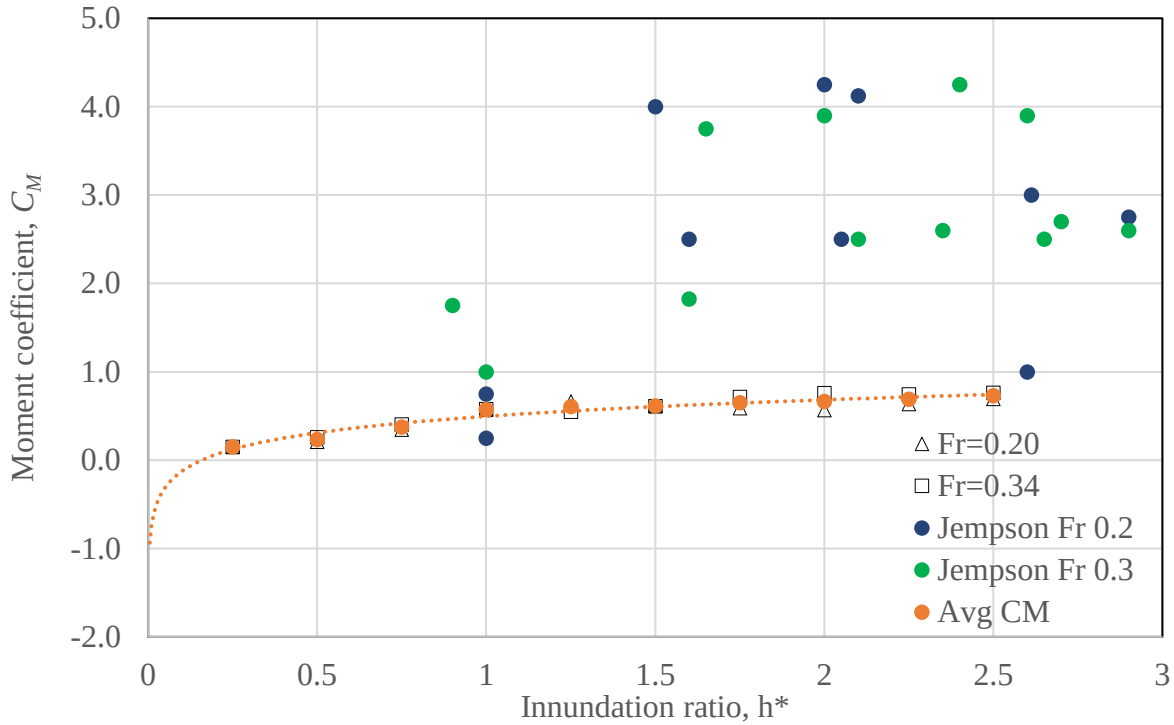

Figure 34- Moment coefficient vs inundation ratio for Bridge Model 2(TX-54 with 46' wide deck)

4.3 Bridge Model 3: BB-15 Slab Beam

26-ft Wide Deck

In Figure 35, the drag coefficient drops from an inundation ratio of 0.25 to 0.75, and then increases to an average value of about 3 across the two Froude numbers tested. Jempson's limited data set for Type B- box' superstructure makes direct comparisons difficult.

The lift coefficient data in Figure 36 is roughly in line with most other experiments. One notable trend is that the lift coefficients for Froude numbers 0.2 and 0.3 begin diverging after the inundation ratio inflection point of 1, which is the opposite of the usual converging pattern.

The moment coefficient results are typical to most of the experiments, with values increasing as the submergence ratios increase (Figure 37).

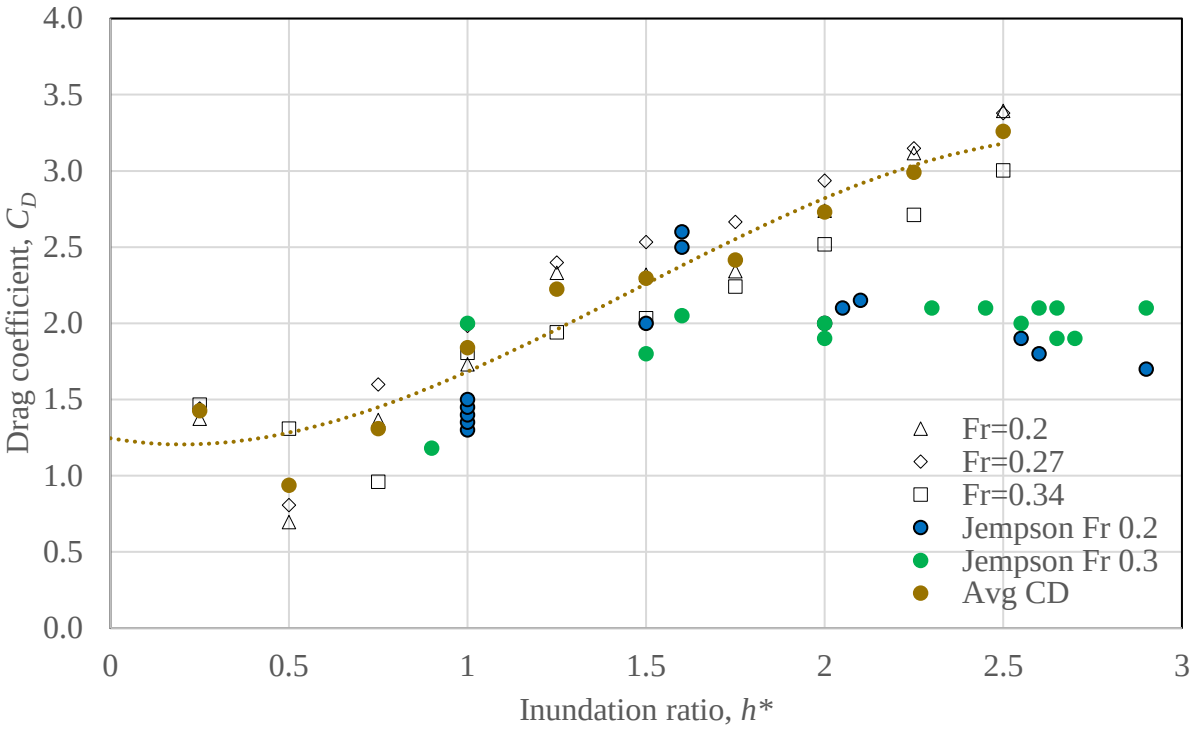

Figure 35-Drag coefficient vs inundation ratio for Bridge Model 3 (Slab Beam with 26' wide deck)

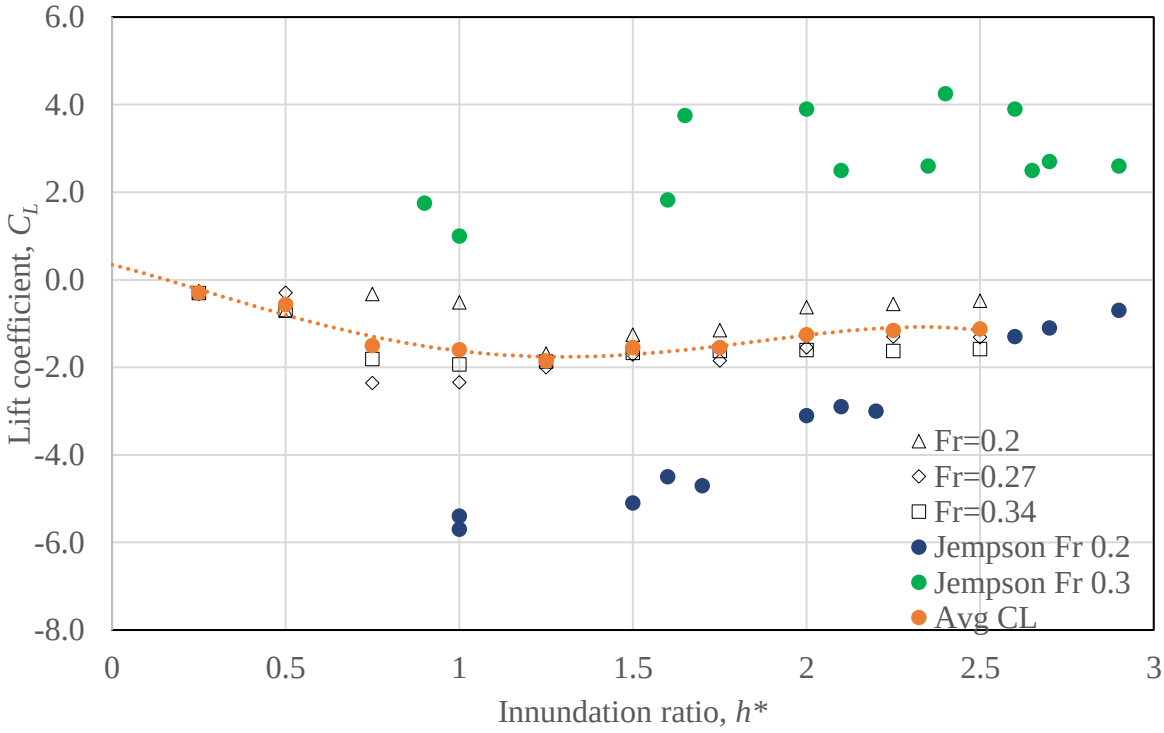

Figure 36- Lift coefficient vs inundation ratio for Bridge Model 3 (Slab Beam with 26' wide deck)

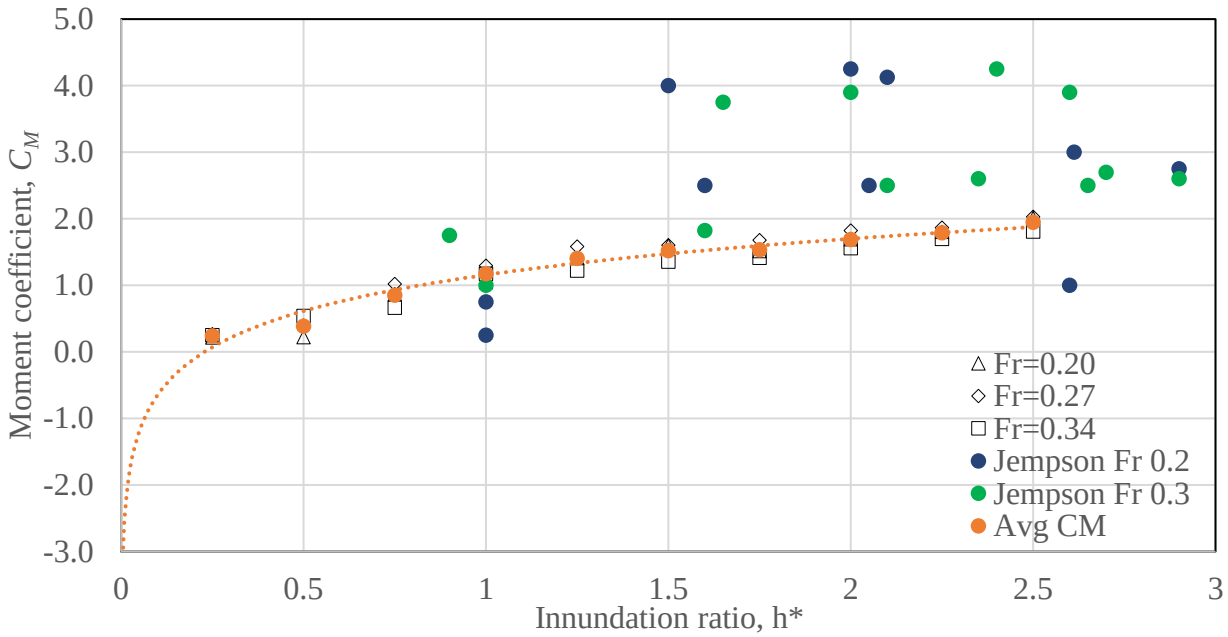

Figure 37-Moment coefficient vs inundation ratio: Bridge Model 3 (Slab Beam with 26'wide deck)

46-ft Wide Deck

In Figure 38, the drag coefficient drops from an inundation ratio of 0.25 to 0.75, and then increases to an average value of about 3 across the two Froude numbers tested. Jempson's limited data set for the B 'box' superstructure makes direct comparisons difficult.

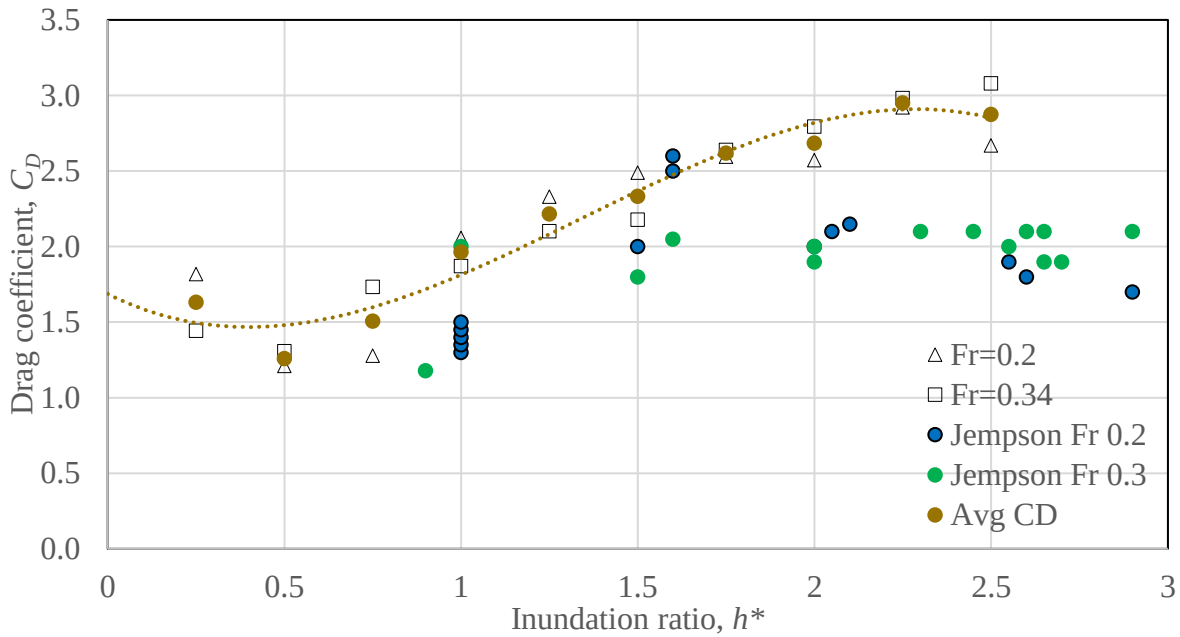

Figure 38-Drag coefficient vs inundation ratio: Bridge Model 3 (Slab Beam with 46'wide deck)

In Figure 39, the difference in lift coefficients leading up to an inundation ratio of 1 between Fr number of 0.2 and 0.3 is interesting, especially because most of the other experiments, including the 26 ft slab beam tests, show that the lift coefficient values diverge more based on inundation ratio than Froude number. However, for this experiment and the Froude number of 0.2, the lift coefficient values actually increase from 0 to 1, instead of the usual trend of decreasing. Some kind of inflection still occurs at the inundation ratio of 1; however, since the inundation ratios drop and fall mostly in line with those of the Fr =0.3 tests after this point.

The moment coefficient results are typical to most of the experiments, with values increasing as the submergence ratios increase (Figure 40).

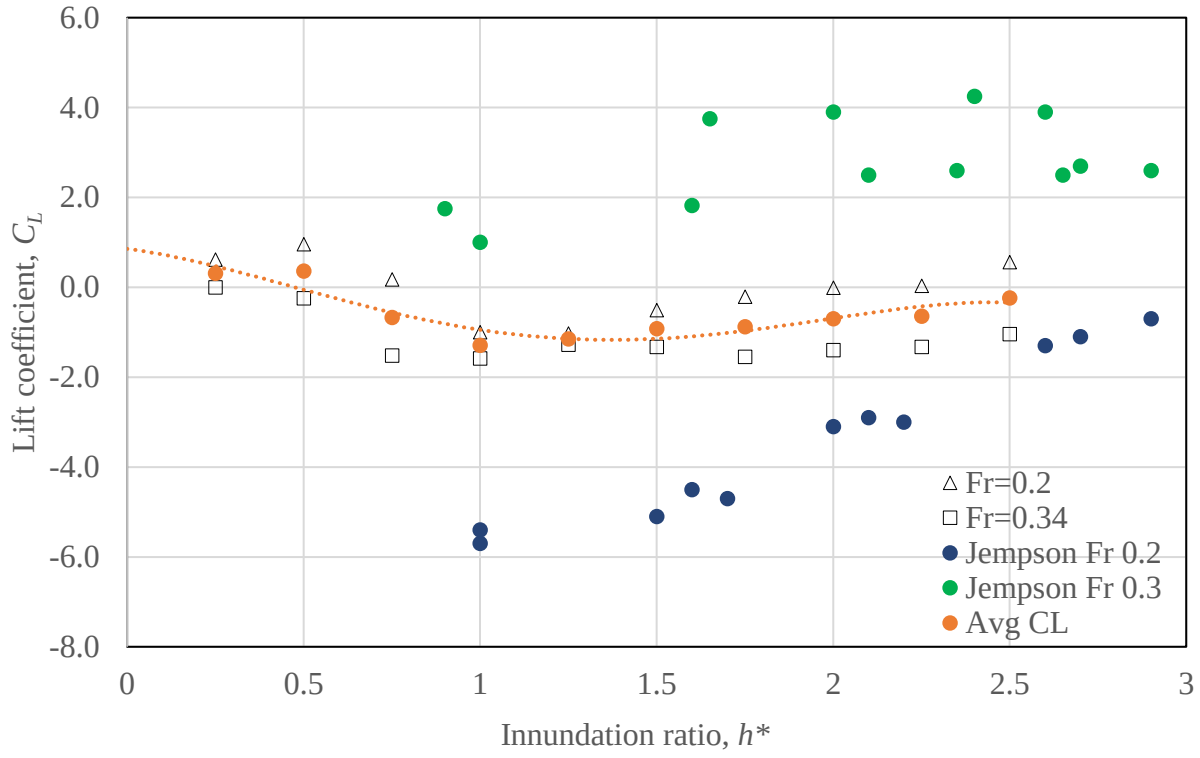

Figure 39-Lift coefficient vs inundation ratio for Bridge Model 3 (Slab Beam with 46’ wide deck)

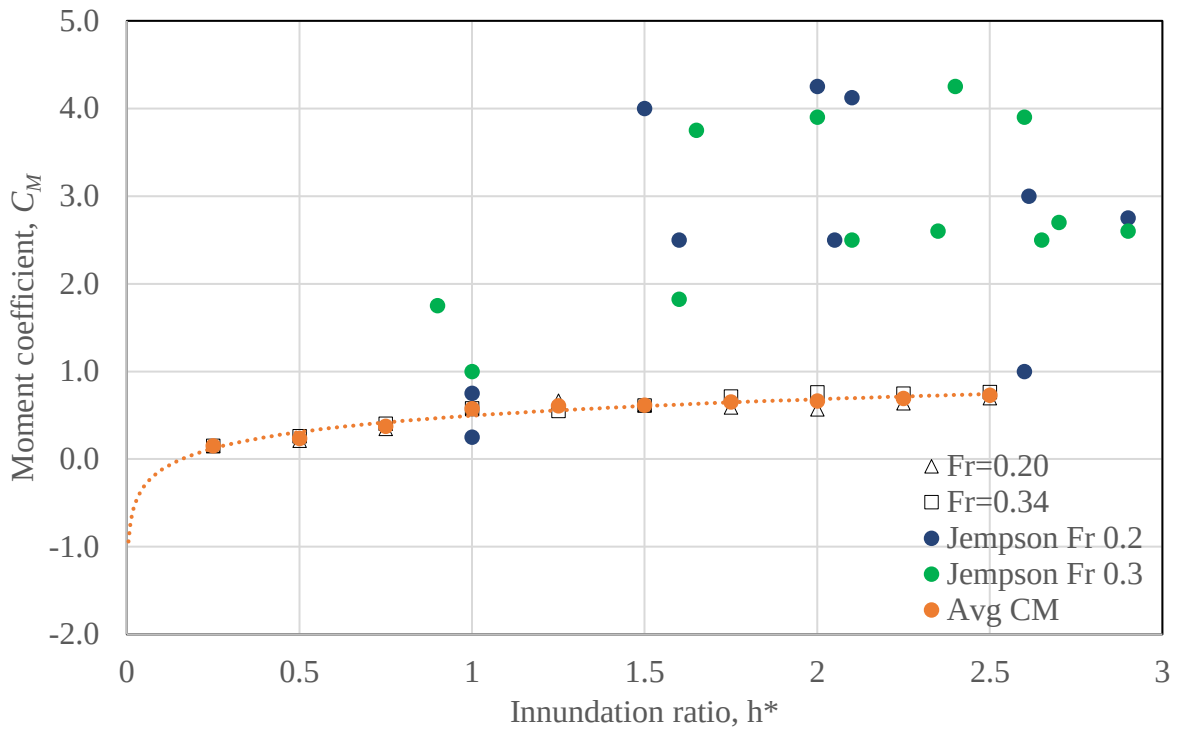

Figure 40-Moment coefficient vs inundation ratio: Bridge Model 3 (Slab Beam with 46'wide deck)

4.4 Bridge Model 4: BB-28 Box Beam

26-ft Wide Deck

In Figure 41, a second-order polynomial relationship between the inundation ratio and drag coefficient can be observed. The drag coefficient rises from a lower to higher inundation ratio, though the drag coefficient values seem to begin plateauing around a ratio of 2, when the flow depth of flow is maximized. This behavior differs from the I-girder decks, where the drag ratio actually decreased then increased over the tested range of inundation ratios. The drop's inflection point also occurs at a lower inundation ratio than in the girder superstructures – at a ratio of 0.5 instead of closer to 1. This increasing pattern also occurs with the Jempson data set, though Jempson did not test inundation ratios below 0.8, so no direct comparison with the initial drag coefficient drop observed in the data set can be made.

The trend of the lift coefficient, decreasing from an inundation ratio of 0.25 to 1, and then increasing again is present for the narrow deck with box beam tests as well. Once again, a comparable plateau seems to occur after a submergence ratio of 2 (Figure 42). Jempson's data was

not taken over a large enough range to correlate this trend, but it is notable that the recorded lift coefficients were much lower than those recorded in this experiment.

As with all other moment coefficient tests performed, Figure 43 shows that the moment coefficient values increased with inundation ratio. In this case, these moment coefficient values were tightly grouped together by Froude number, and varied more widely based on their Froude number.

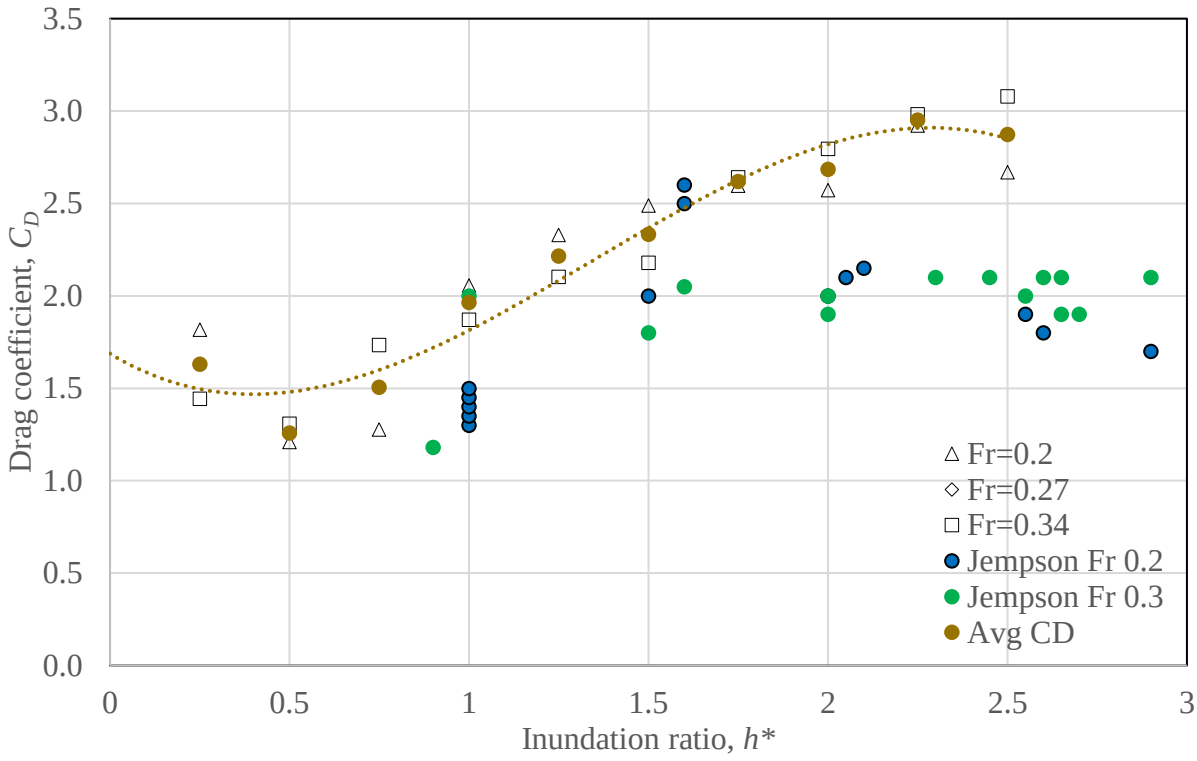

Figure 41- Drag coefficient vs inundation ratio for Bridge Model 3 (Box Beam with 26' wide deck)

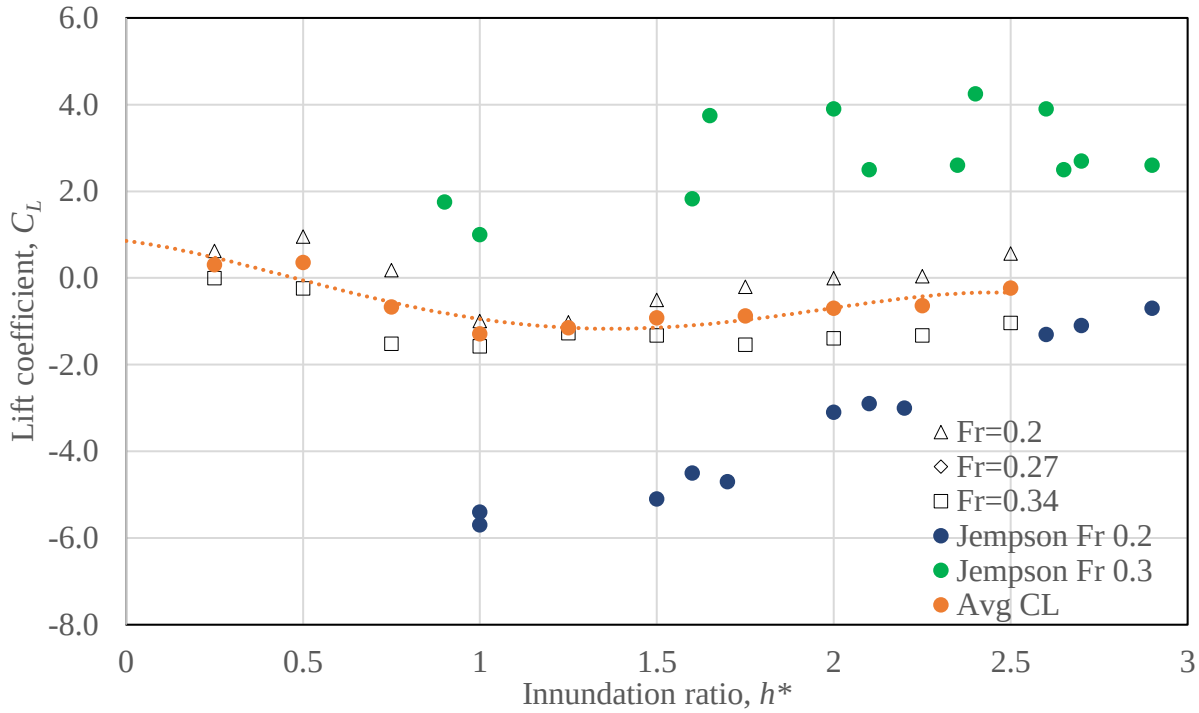

Figure 42- Lift coefficient vs inundation ratio for Bridge Model 3 (Slab Beam with 26' wide deck)

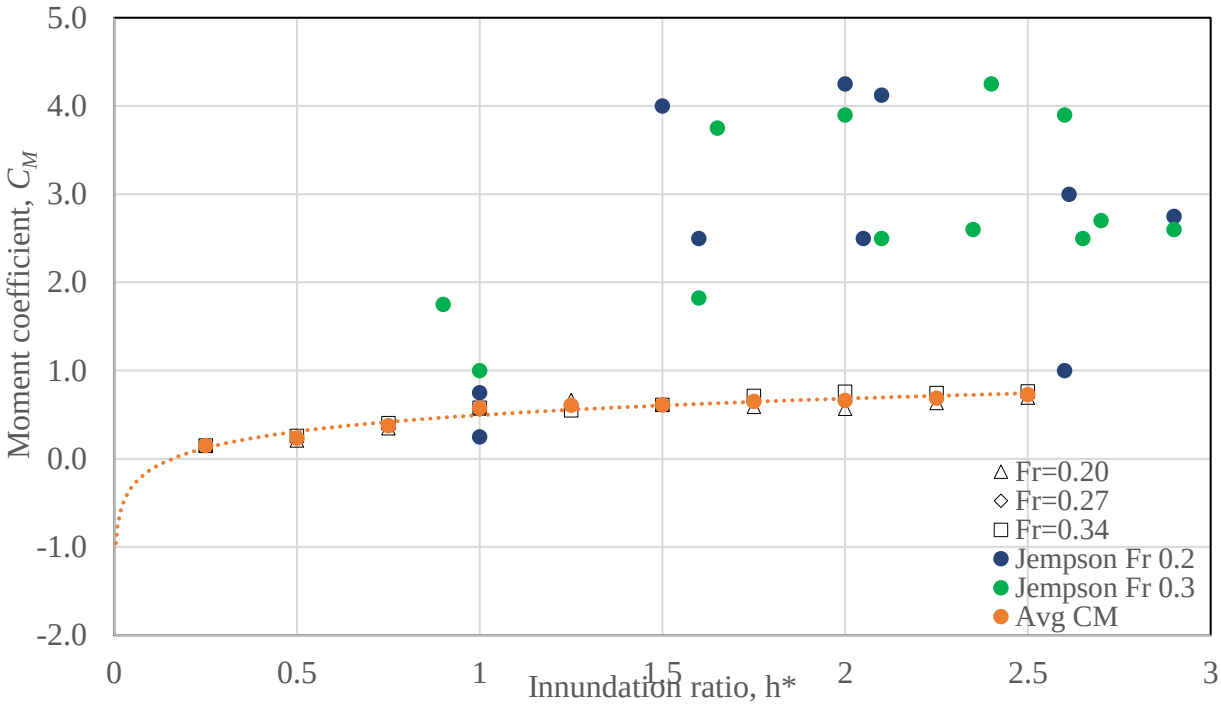

Figure 43- Drag coefficient vs inundation ratio for Bridge Model 4 (Box Beam with 26' wide deck)

44-ft Wide Deck

The wider deck with box beams showed the same interesting data set with respect to its drag coefficient data (Figure 44) as the shorter 26 ft deck test did. Instead of the drop in drag coefficient occurring at an inundation ratio of 1 like I-girders, it occurred at a point closer to an inundation ratio of 0.5. Since the railing design is the same for all beam and girder types, this inflection point difference helps to give some idea of the effect that the girders' more complex bottom surface plays in its hydrodynamics.

The lift coefficient data in Figure 45 below falls in line roughly with most of the other experimental data, with an increase in lift coefficients after an inundation ratio of 1. However, the Fr=0.34 data does not begin increasing after this point, which is interesting, as this behavior does not seem to occur for many other configurations.

The moment coefficient results are typical to most of the experiments, with values increasing as the submergence ratios increase (Figure 46).

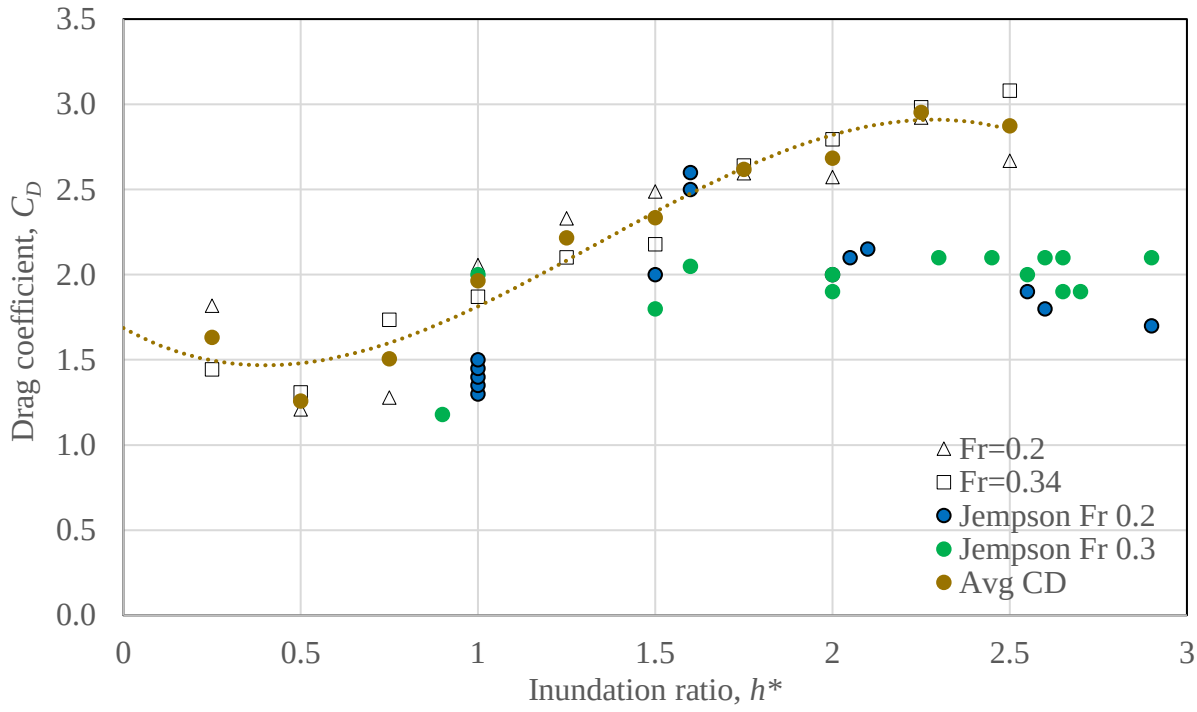

Figure 44- Drag coefficient vs inundation ratio for Bridge Model 4 (Box Beam with 46' wide deck)

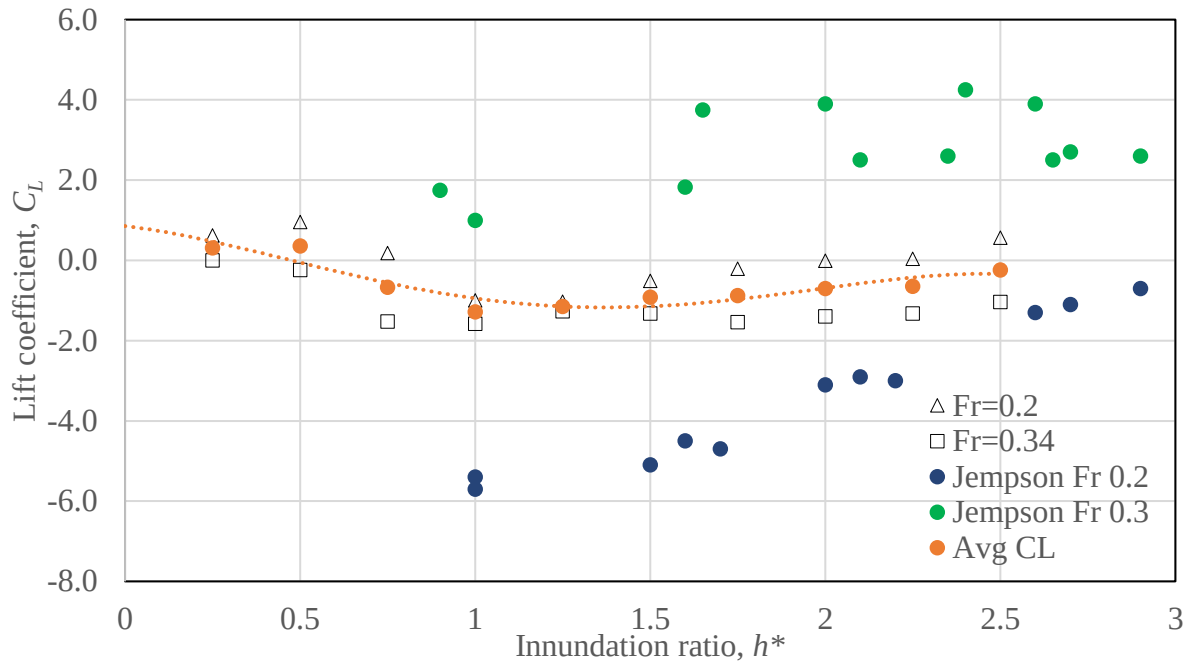

Figure 45- Lift coefficient vs inundation ratio for Bridge Model 4 (Box Beam with 46' wide deck)

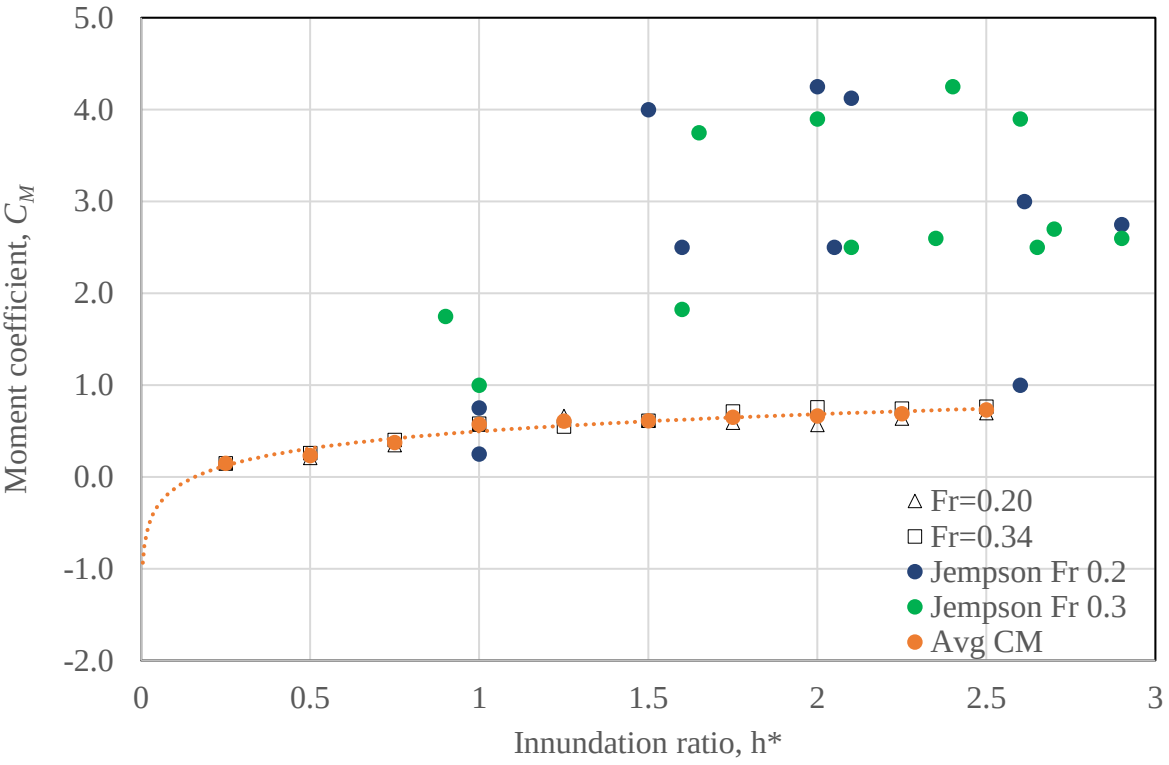

Figure 46-Moment coefficient vs inundation ratio: Bridge Model 4 (Box Beam with 46'wide deck)

4.5 Debris Experiments

4.5.1 Flat Plate

Relative to the TX54, tests without debris run at the same Froude number, the flat plate begins with a lower drag coefficient and increases as the inundation ratio increases, unlike the debris-free case, which exhibits the falling then rising drag coefficients noted earlier in the results (Figure 47). The debris plate's obstruction appears to eliminate some of the hydrodynamic interplay caused by the girder structure, instead replacing it with a relationship where the drag coefficient increases as the inundation ratio increases.

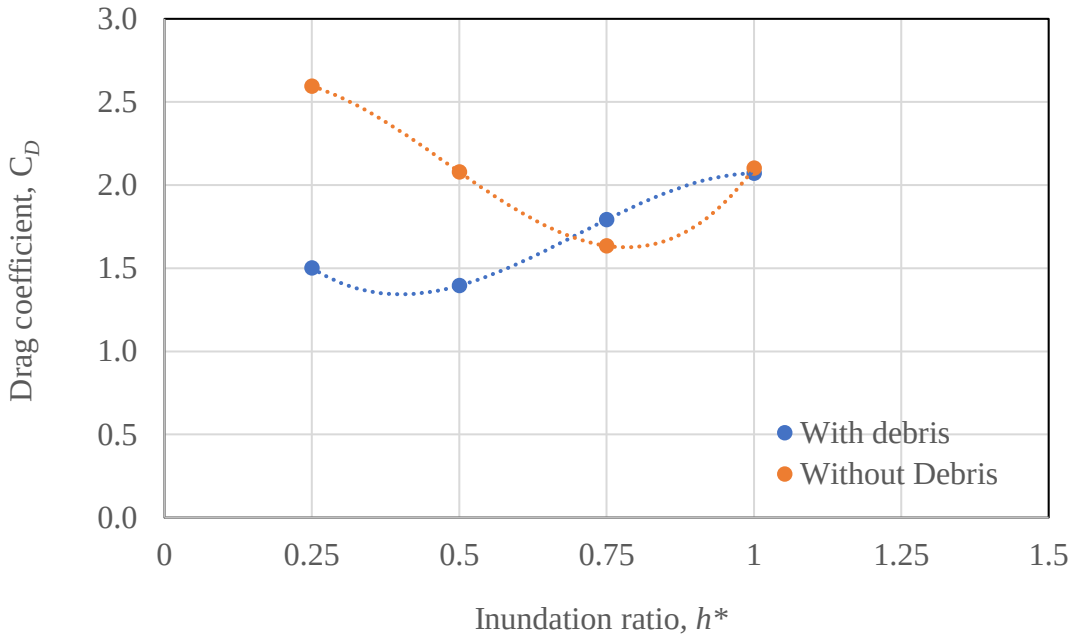

Figure 47- Debris Flat Plate Drag Coefficient vs Inundation Ratio

4.5.2 Debris Mat Wedge

The presence of the debris mat wedge reduces the drag coefficients relative to the flat plate only at greater submergence ratios (Figure 48).

The presence of the buoyant debris mat attached to the bridge deck resulted in a smaller difference in drag coefficient values relative to the debris-free test conditions (Figure 49).

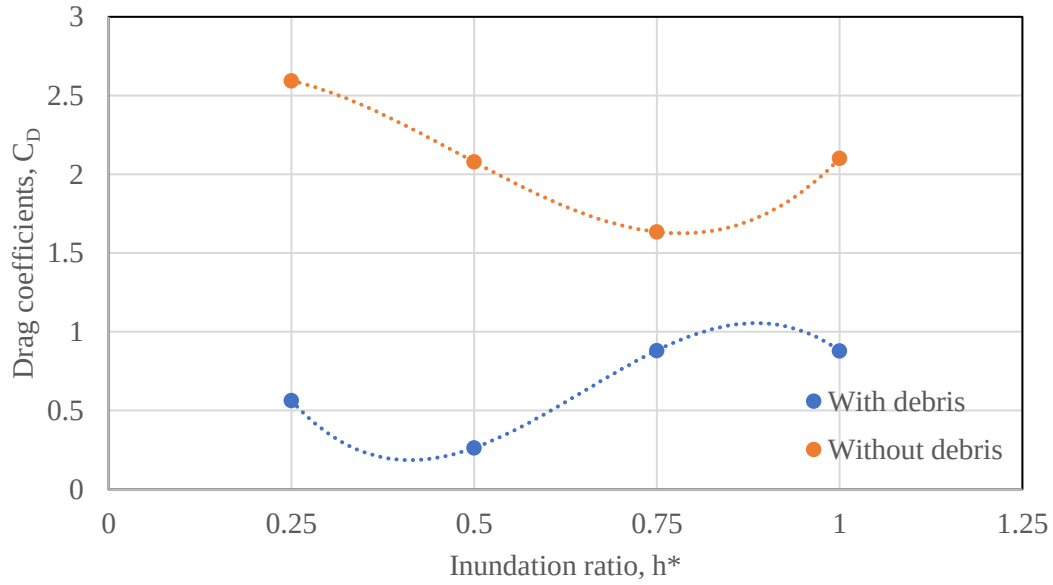

Figure 48- Debris Mat Fixed Wedge Drag Coefficient vs Inundation Ratio

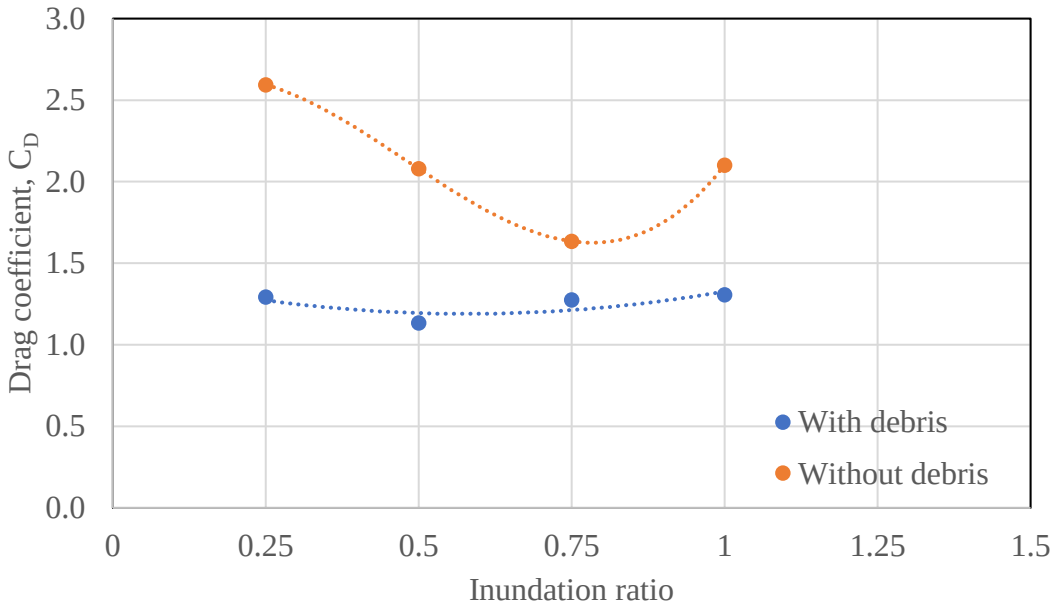

Figure 49- Debris Mat Buoyant Wedge Drag Coefficient vs Inundation Ratio

Chapter 5 Discussion

The discussion is divided into four parts: examining trends in the drag, lift, and moment coefficients as well as the debris results. The plots are made up of the combined bridge deck results for each tested set of Froude numbers, i.e. 0.2, 0.27, and 0.34. Each section consists of commentary accompanying plots of the evaluated force coefficients, including hypothesis for the observed trends.

5.1 Drag Coefficient

The combined drag coefficient plot for the Froude number = 0.2 flow scenario shown in Figure 50 which is fitted with a third-order polynomial line to describe the relationship between the drag coefficient and the inundation ratio. The line has been fit to the average of all drag coefficient values and has an R^2 value of 0.92 indicating that the data follows the fitted third-order polynomial line to a statistically-significant degree.

This fitted polynomial described a decreasing then increasing drag coefficient pattern that inverts at an inundation ratio of 0.8. The coefficients then level out as the inundation ratio reaches 2. Reasons for the 0.8 inundation ratio inversion could have to do with the interaction between the partially-submerged bridge deck and railing that occurs during this point. It is important to note that even though the railing is not totally submerged, water can overtop the bridge deck due to the drainage holes at the bottom of the railing on the full-scale bridge protypes, or the necessary clearance between the edge of the bridge deck and the wall of the flume in the model.

The Froude number = 0.27 scenario shown in Figure 51 shows similar trends: a drag coefficient inflection point at an inundation ratio of 0.8, and a leveling off in drag coefficient as the inundation ratio reaches 2. The third-order polynomial line of best fit – fitted to the middle of the data distribution TX-28 bridge- has an almost identical R^2 value of 0.93, indicating that this data can also be described by the polynomial distribution pattern with a high degree of confidence. While the shape of the drag coefficient curve is similar to the lower-Froude number scenario, the distribution of the Froude numbers is tighter, ranging from 0.7 to 3.4, suggesting that as the flow rate increases, it begins to play a larger role in determining drag coefficients relative to the girder geometry.

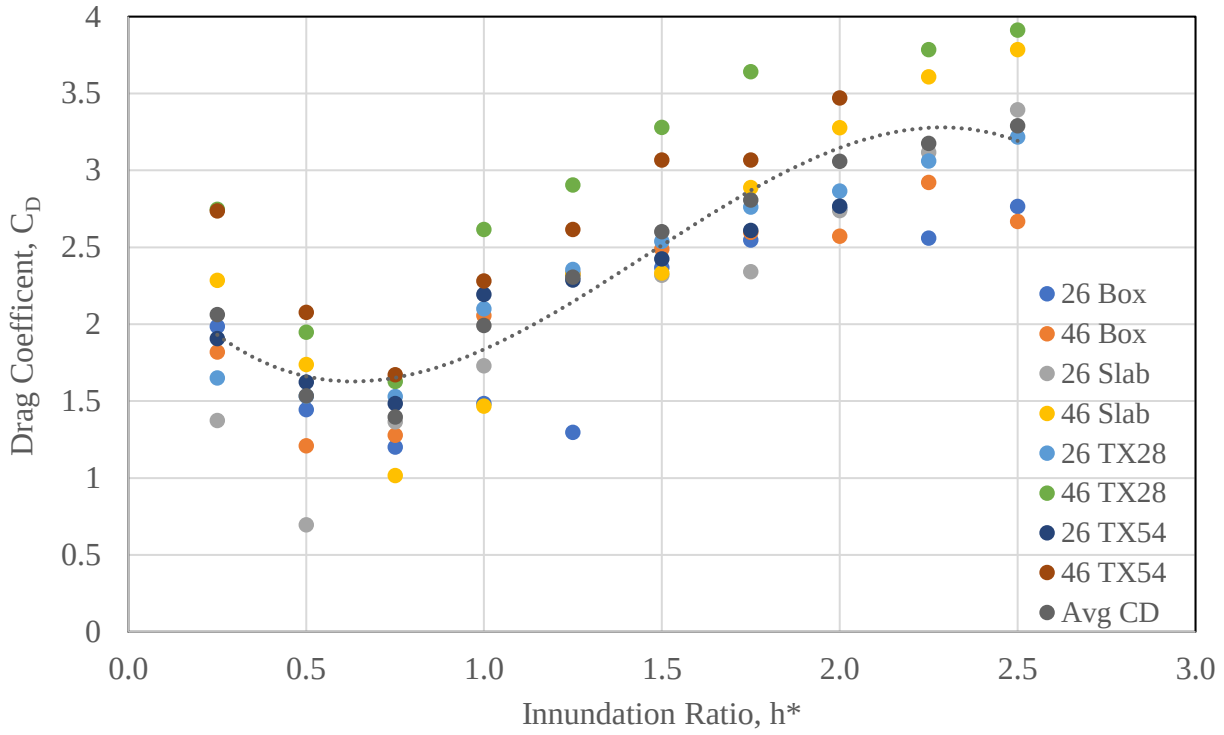

Figure 50- Drag coefficient vs inundation ratio for all bridge decks at Froude number 0.20

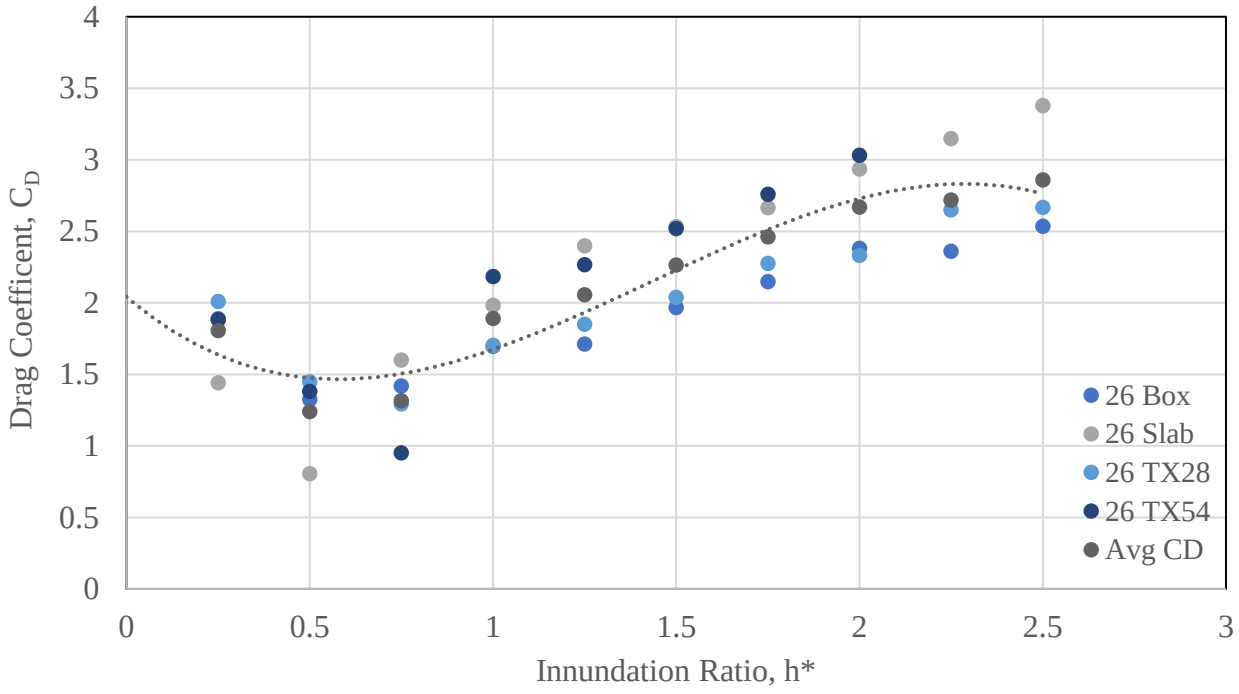

Figure 51- Drag coefficient vs inundation ratio for all bridge decks at Froude number 0.27

In Figure 52, the Froude number = 0.34 flow scenario, the drag coefficient inflection point appears to shift to an inundation ratio of 0.5 for the lower-profile 26’ deck with box and slab beams data sets, while all the other tested bridge sections maintained an inflection point at 0.8, suggesting that something about the particular geometry of these decks becomes significant at higher flow rates. The rest of the bridge decks follow the same trends as the lower Froude number scenarios.

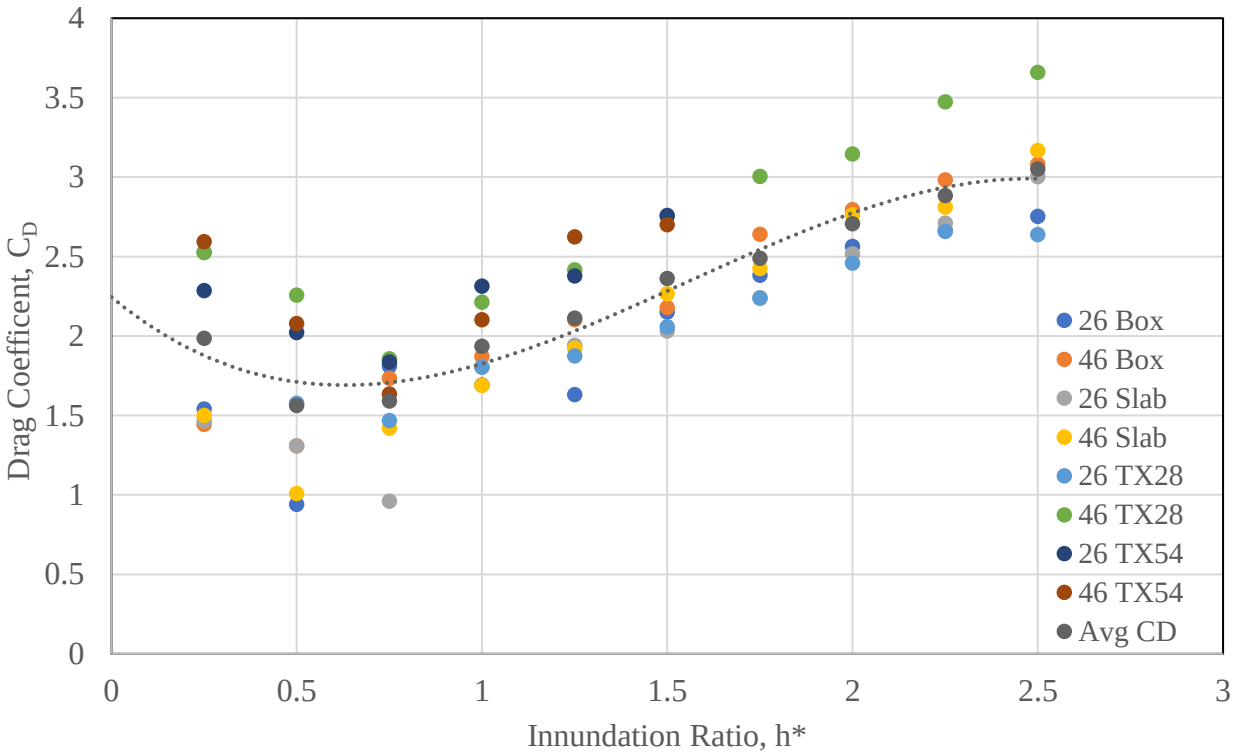

Figure 52- Drag coefficient vs inundation ratio or all bridge decks at Froude number 0.34

These combined plots, taken together, indicate that something significant is occurring at an inundation ratio of 0.8 and that the effects of this interaction are consistent across varying flow scenarios, demonstrating just how significant bridge geometry can be. One more point to note is how the drag coefficient values began to level off as the inundation ratio exceeded 2.0, which suggests a minimum set of depths for which the localized effects of the bridge section become less significant in terms of overall channel flow.

The exact mechanics of the overtopping at an inundation ratio of 0.8 cannot be known exactly with the current experimental arrangement, though conducting a PIV study could provide additional velocity datapoints that might help narrow them down. One likely scenario is that as water begins

to infiltrate the bridge deck, through drainage holes on upstream railing of life-size bridges, or around the edges of the railing in the laboratory model, it begins moving across the top of the bridge deck until comes into contact with the downstream railing, leading to drag force being encountered both directly from the overtopping water's impact against the downstream railing, as well as from the additional frictional resistance encountered by the water's travel along the upper surface deck.

5.2 Lift Coefficient

The Fr= 0.2, lift coefficient data also displays a polynomial data distribution, though with a larger spread of drag coefficients (Figure 53). One thing that all data sets do have in common, however, is the lift coefficient inflection point, which consistently occurs at an inundation ratio of 1.0 across all the bridge decks. The interaction between channel flow overtopping the just-totally submerged upstream and downstream railing must be significant. Further testing around this ratio could be revealing.

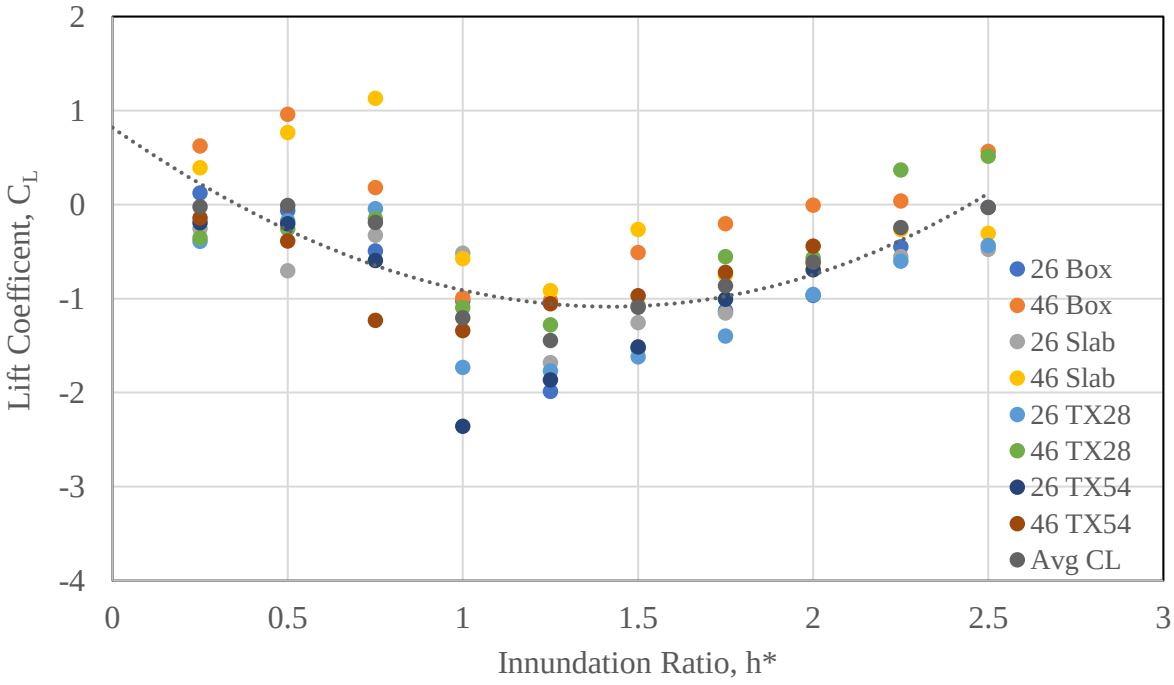

Figure 53- Lift coefficient vs. inundation ratio for all bridge decks at Froude number 0.2

As evident in Figure 54, the inundation ratio inflection point of 1 still holds true in the Froude number = 0.27 flow scenario. The lift coefficient values appear to diverge even more sharply at this point than that as evident at the lower flow scenario, suggesting that the inundation ratio of 1

geometry becomes even more significant at higher flow rates. The larger amount of divergence between lift coefficient data points at the higher flow rate may indicate that differences in the uplift caused by girder geometry become more pronounced as the flow rate increases. While only the short-decked bridges were tested in this scenario due to time constraints, the results from Figures 52 and 54 suggest that the longer-length decks would follow similar trends.

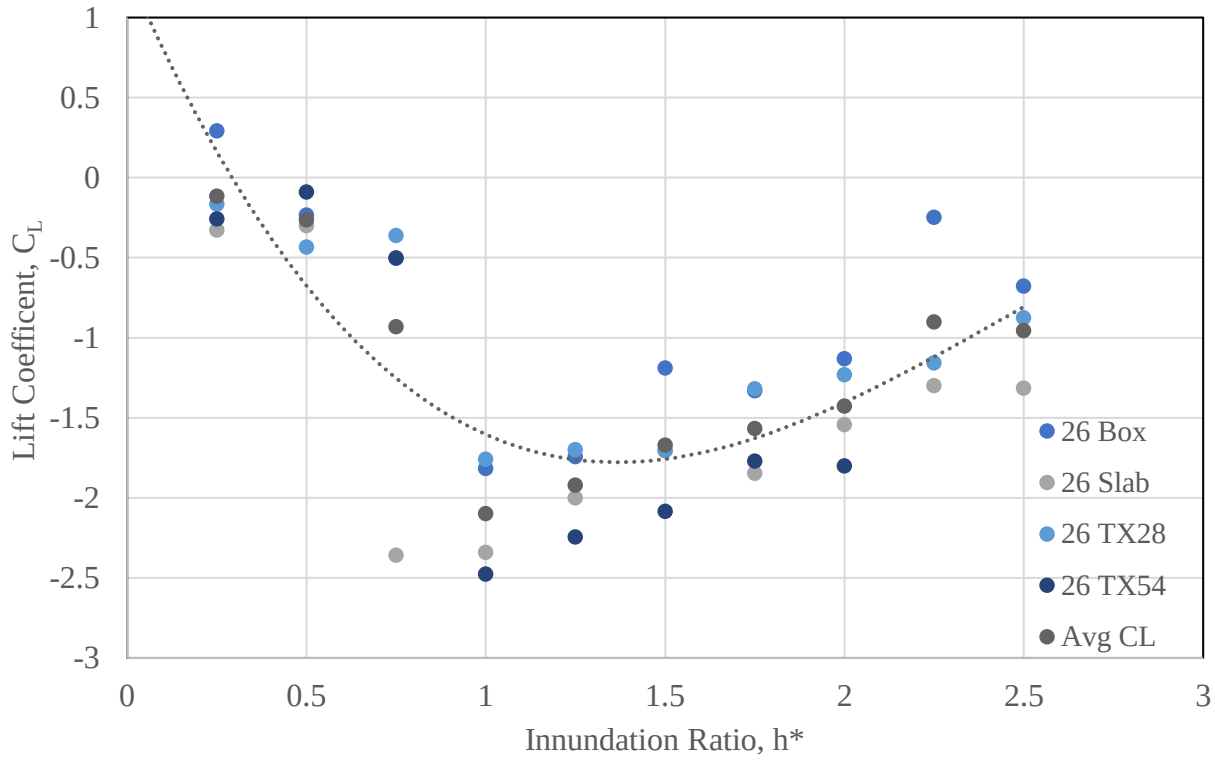

Figure 54- Lift coefficient vs inundation ratio for all bridge decks at Froude number 0.27

The lift coefficient inundation ratio inflection point stays at 1.0 for the Froude number = 0.34 scenario (Figure 55), indicating that the position of the lift coefficient inflection point is not strictly dependent on the Froude number of the flow scenario. As will be considered later in this discussion, this point in important with respect to the Froude number constraints of this research.

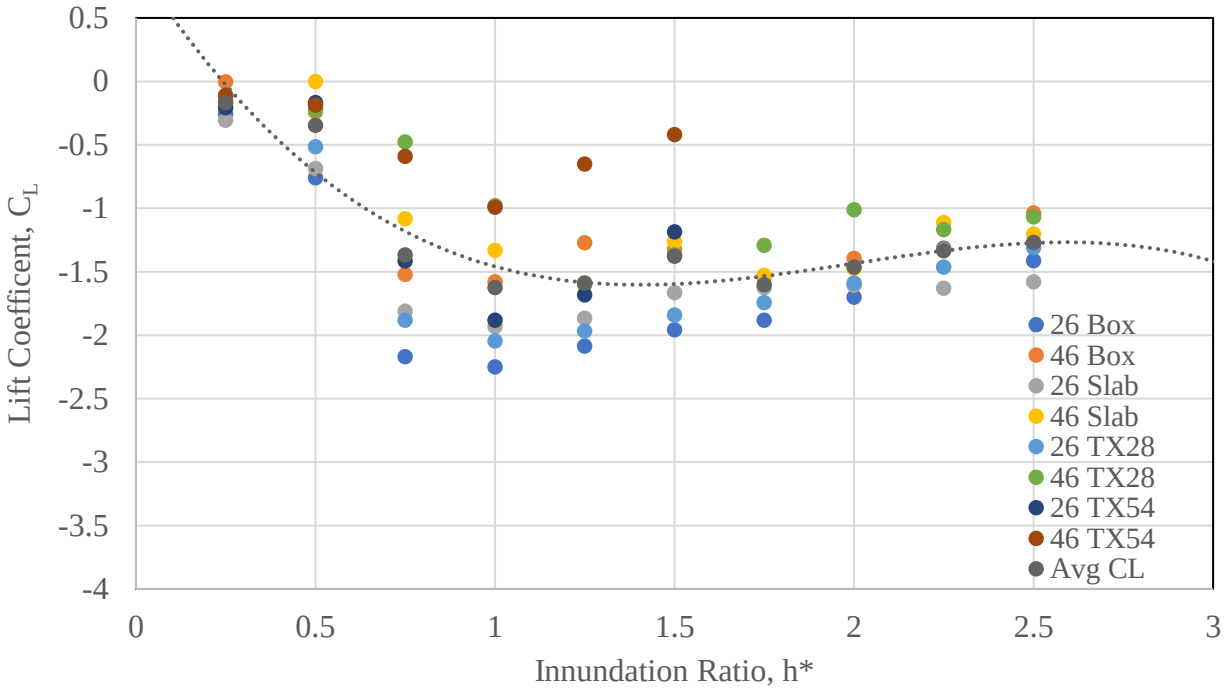

Figure 55- Lift coefficient vs inundation ratio for all bridge decks at Froude number 0.34

The lift coefficient's consistent value inflection point of 1.0 should be investigated further in order to better understand the mechanics involved. If the railing being overtopped is truly a significant criterion in the location of this inflection point, then performing a set of experiments with an altered railing height could help confirm or at least better understand this hypothesis.

5.3 Moment Coefficient

The moment coefficient values appear to fall into several bands depending on bridge length, with the 46' wide bridge sections, having a lower range of moment coefficients than the 26' wide sections. The curve fit to both sections was logarithmic with an R-squared value of 0.93 for the curve fitted to the average of all data sets, suggesting that a logarithmic distribution describes the data reasonably well (Figure 56).

The moment coefficient divergence based on deck width is likely due to the longer bridges' larger mass, which is providing additional inertia for the hydraulic forces to overcome.

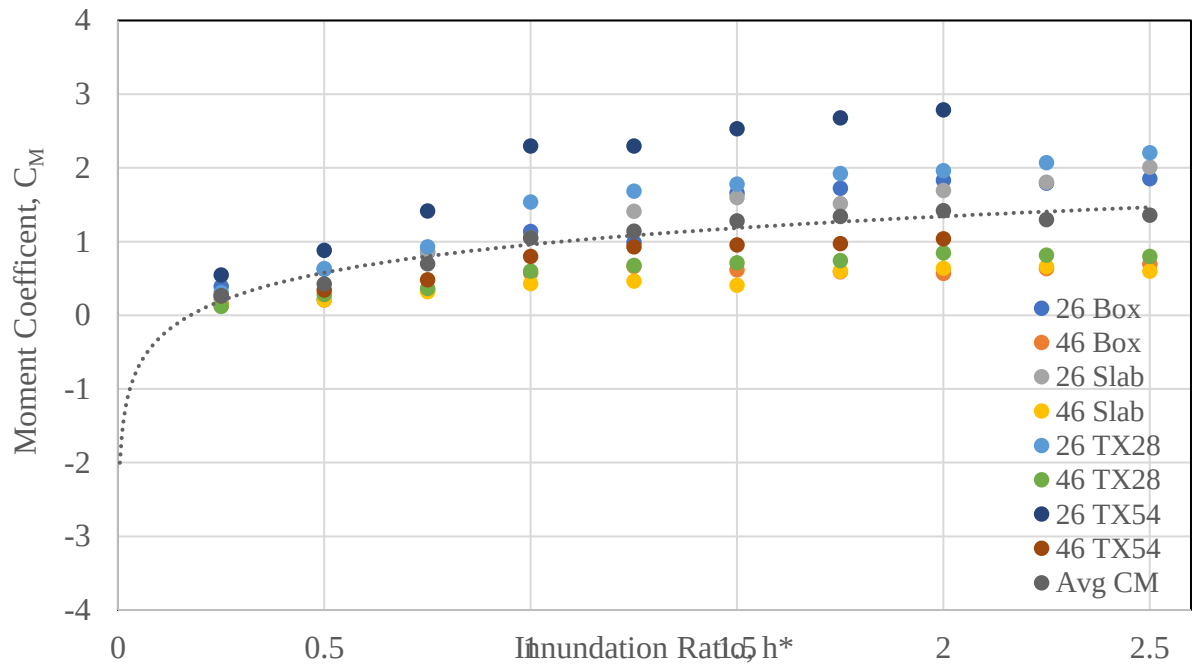

Figure 56- Moment coefficient vs inundation ratio for all bridge decks at Froude number 0.20

Only the short 26' bridge decks were investigated for the Froude number 0.27 scenario, while all data can be fit with a logarithmic trend line, as seen in Figure 57, the differences caused by the geometry of the higher-profile TX54 girders relative to the other superstructures can be observed, and for this reason, these data points have been fit with their own distinct logarithmic trend line.

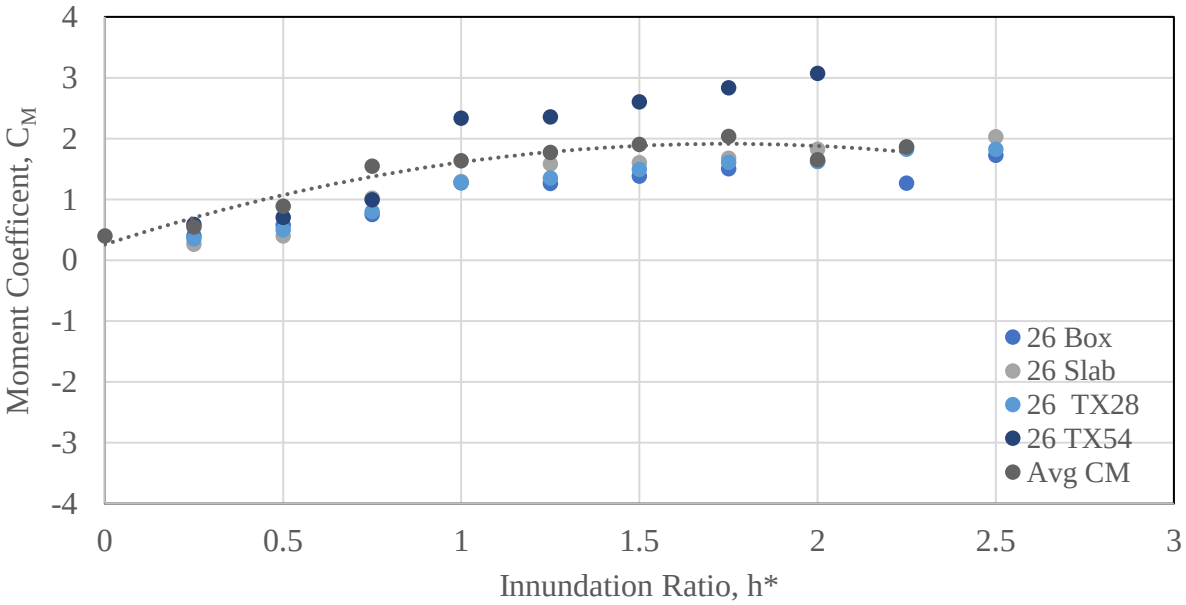

Figure 57- Moment coefficient vs inundation ratio for all bridge decks at Froude number 0.27

The 26’ wide bridge deck with TX54 in Figure 58 has an especially high moment coefficient, suggesting that at higher Froude numbers, higher-profile superstructures are exposed to higher moments. The distinct ‘bands’ of grouped logarithmically-distributed moment coefficient values prominent at lower Froude numbers are here much less visible, suggesting that the impact of bridge girder spacing and layout is reduced as the Froude number increases.

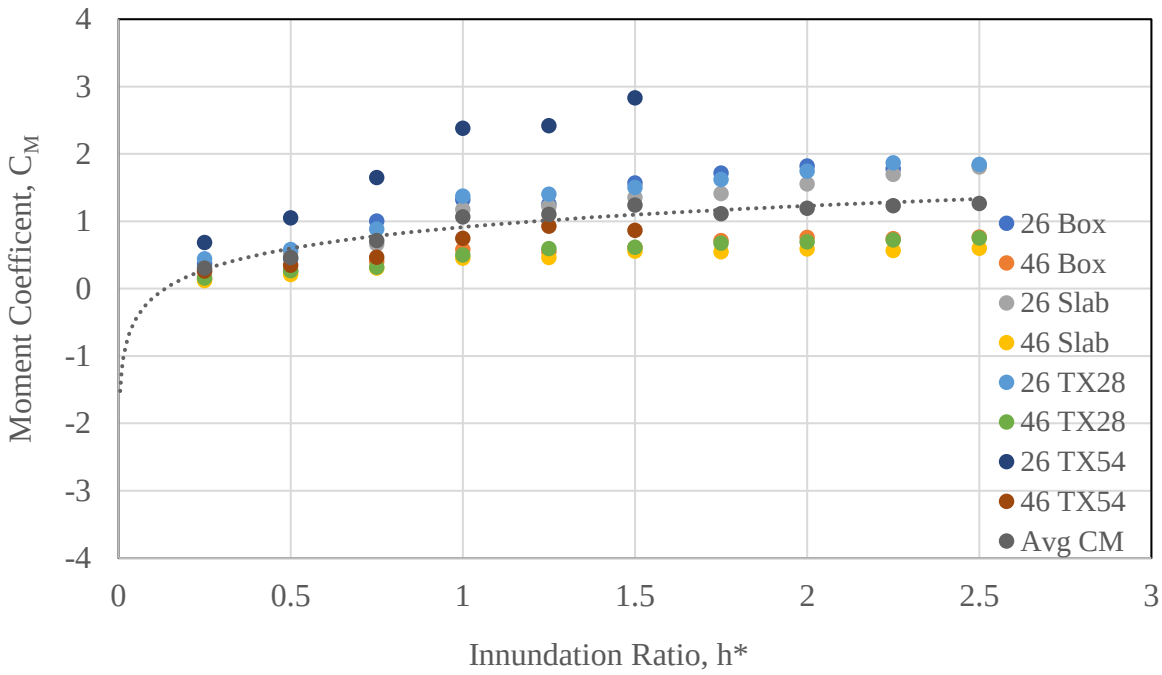

Figure 58- Moment coefficient vs inundation ratio for all bridge decks at Froude number 0.34

While the results of the analysis of 598 TxDOT bridges showed an average Froude number of 0.39, with many bridge channels exceeding that amount- up to 1.3 (Hummel and Pervaiz 2020), the ability of the test flume to generate Froude numbers of no greater than 0.34 was not too great of an obstacle because the location of the drag and lift coefficient inflection points at inundation ratios 0.8 and 1.0 respectively, and because the coefficient values did not increase notably at higher Froude numbers.

This trend can be better reinforced with reference to Jempson (2000) - see Figure 59 below, where Froude numbers up to 0.50 were evaluated for a girder-type bridge superstructure model, and the maximum drag coefficient values stayed flat as the Froude number increased. In this figure, the maximum drag coefficient value at a Froude number of 0.2 is 2.2, also its value at a Froude number of 0.5.

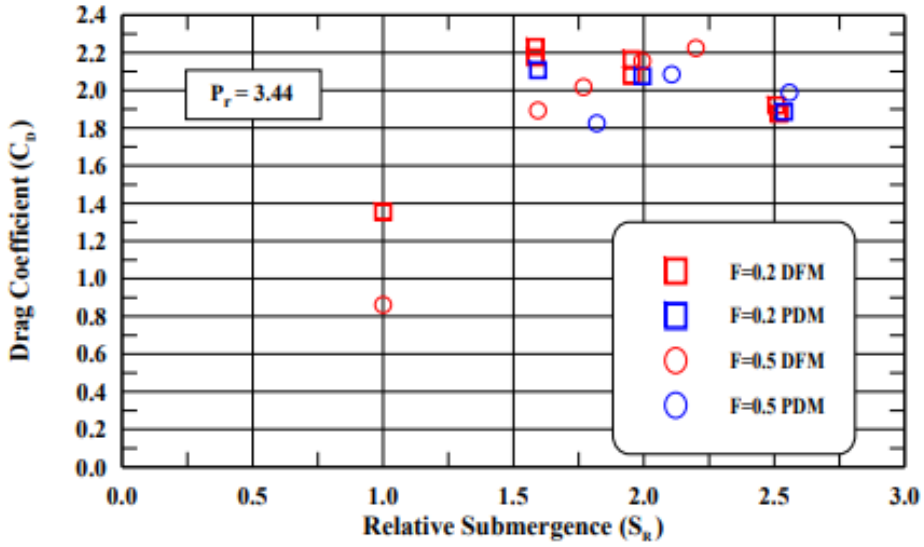

Figure 59- drag coefficient vs inundation ratio comparison (Jempson, 2000).

Evaluation of the average of all bridge types' drag, lift and moment coefficients across an average of the Froude numbers helps to illustrate these trends. Evaluating the drag coefficient values (Figure 60), shows us that the 0.20 Froude number drag coefficient values are actually greater than the higher 0.34 Froude number values, while the drag coefficient inflection point occurs at an inundation ratio of 0.8 across all three sets of Froude numbers. As noted previously, the data sets follow a third-order polynomial distribution across the range of evaluated inundation ratios.

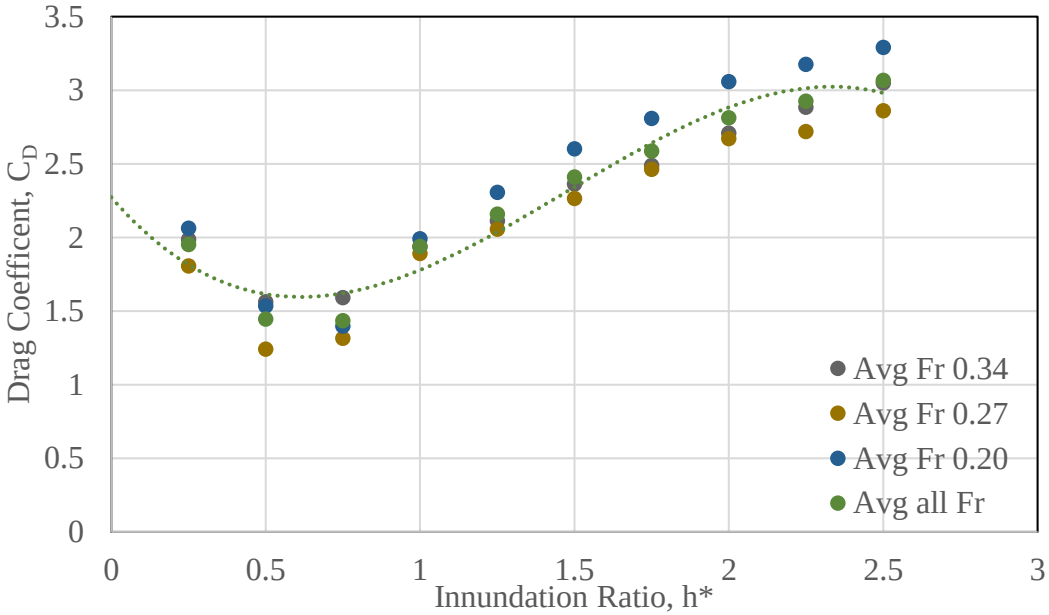

Figure 60- Average drag coefficients vs inundation ratio for all bridge deck types and Froude numbers

Likewise, the averaged lift coefficient values show similar trends (Figure 61) with the averaged inflection point occurring at an inundation ratio of 1.0 across all three data sets. These trends demonstrate that the limitations in the laboratory flume's ability to achieve higher Froude numbers are not insurmountable when evaluating general trends in coefficient distributions- the drag and lift coefficients all shared similar inflection points across all tested Froude numbers, and Jempson's research indicates that this trend should hold true even for higher Froude number values.

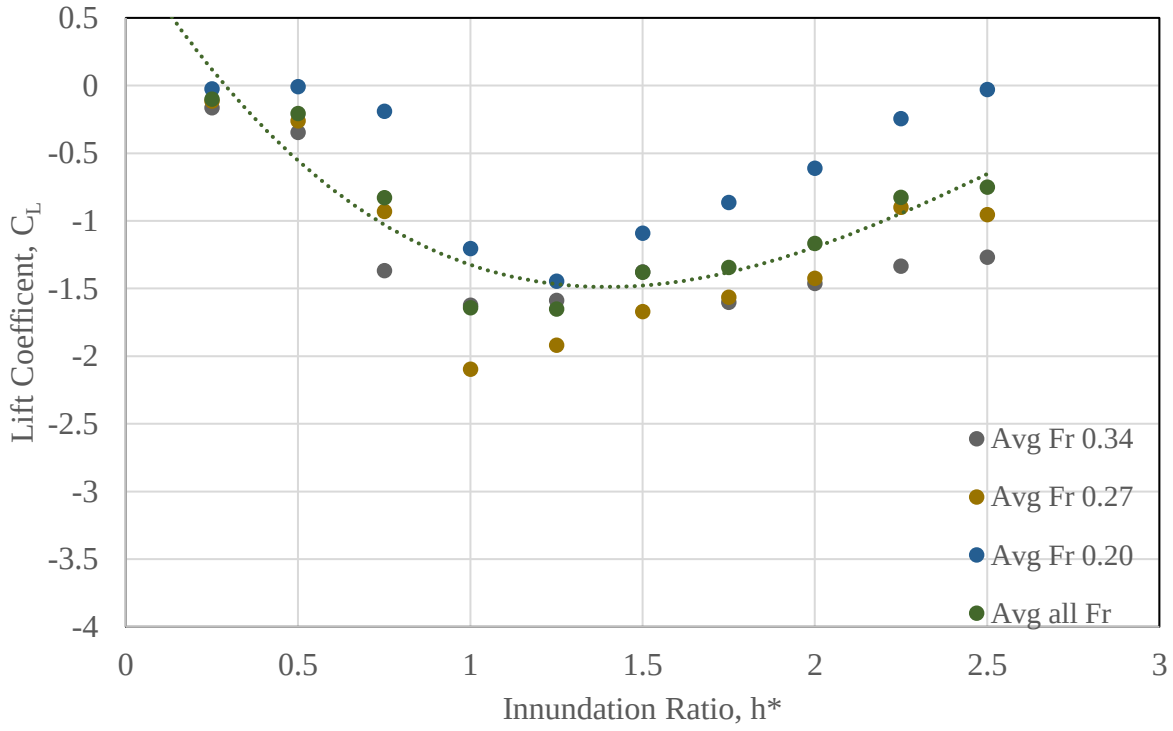

Figure 61- Average lift coefficients vs inundation ratio for all bridge deck types and Froude numbers

The average moment coefficient values for 26' wide decks shown in Figure 62 demonstrate a similar principle – noting that only 26' wide decks were considered for this plot since, as previously noted, bridge deck width has a considerable impact on the moment coefficient, so only 26' wide decks could be considered for this comparison, since they are the only lengths measured across all three Froude numbers. The average moment coefficients are very tightly grouped, demonstrating that bridge geometry variances, specifically bridge length and superstructure height, play a more significant role in moment coefficients than Froude number.

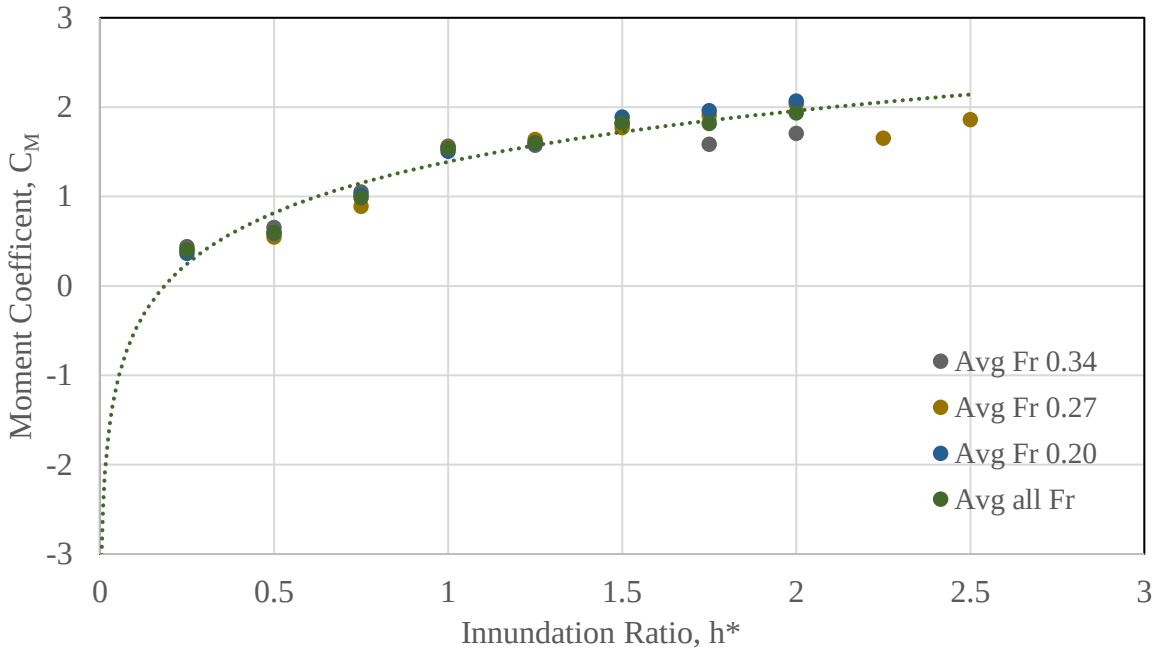

Figure 62- Average moment coefficients vs inundation ratio for 26' decks all Froude numbers

These results show that some useful information regarding coefficient loading patterns can still be determined by researchers who may not be able to generate a full set of flow scenarios at Froude numbers that would be encountered in the field.

5.4 Debris

The debris experiments demonstrated a definite divergence in drag coefficient values between the presence and absence of debris, as presented previously in Figures 47 and 48. Relative to the TX 54 tests without debris run at the same Froude number, the flat plate begins with a lower drag coefficient, and increases as the inundation ratio increases, unlike the debris-free case, which exhibits the falling then rising drag coefficients noted earlier in the results (Figure 47). The debris plate's obstruction appears to eliminate some of the hydrodynamic interplay caused by the girder structure, instead replacing it with a relationship where the drag coefficient increases as the inundation ratio increases.

Chapter 6: Conclusion and Future Work

6.1 Summary

The largest and smallest drag, lift, and moment coefficient values for four bridge model tested in this study are summarized in Tables 5 to 8.

Table 5- Summary of drag, lift and moment coefficient for Bridge Model 1: TX-28

TX 28	26 ft Wide Deck		46 ft Wide Deck	
Coefficient	High	Low	High	Low
C_D	3.2	1.3	4.0	1.6
C_L	-0.04	-2.0	0.5	-1.6
C_M	2.2	0.3	0.8	0.1

Table 6- Summary of drag, lift and moment coefficient for Bridge Model 1: TX-54

TX 54	26 ft Wide Deck		46 ft Wide Deck	
Coefficient	High	Low	High	Low
C_D	3.0	0.9	3.4	1.6
C_L	-0.08	-2.4	-1.3	-0.1
C_M	3.1	0.5	1.0	0.2

Table 7- Summary of drag, lift and moment coefficient for Bridge Model 3: SB-15 Slab Beam

Slab Beam	26 ft Wide Deck		46 ft Wide Deck	
Coefficient	High	Low	High	Low
C_D	3.6	0.7	3.7	1.0
C_L	-0.08	-2.3	1.1	-1.6
C_M	2.0	0.2	0.6	0.1

Table 8- Summary of drag, lift and moment coefficient for Bridge Model 4: BB-28 Box Beam

Box Beam	26 ft Wide Deck		46 ft Wide Deck	
Coefficient	High	Low	High	Low
C_D	2.8	0.9	3.7	1.0
C_L	0.2	-2.2	1.1	-1.5
C_M	1.8	0.3	0.6	0.1

6.2 Conclusion

A series of experiments was conducted in the laboratory to study hydrodynamic forces on bridge superstructures during flood events. The 1:50 scale models of the Texas Department of Transportation's typical reinforced concrete bridge superstructures were tested in these experiments, with the overarching objectives of:

- Documenting the hydrodynamic forces affecting four types of Texas Department of Transportation (TxDOT) highway bridge girder types across three Froude number flow and a range of submergence scenarios in a laboratory test flume
- Calculating the coefficients of drag, lift, and moment and compare them with previous studies.

The experiments were performed at Froude numbers of 0.20, 0.27, and 0.34 over a range of inundation ratios from 0 to 2.5. The key findings of this experiment are the following:

- Effects of inundation ratio: It appeared that inundation ratio is the single greatest factor in determining the inflection point of the drag and lift coefficients- 0.8 for the drag coefficients and 1.0 for the lift coefficients. This finding seems significant and definitely bears consideration for further work
- Effects of Fr number: The location of the drag and lift coefficient inflection points seemed to be largely independent of Froude number, suggesting that practical testing, even at Froude numbers below field conditions has some merit. The presence of debris increased the observed drag coefficients for a given Froude number.
- Effects of bridge width: The bridge width seemed to have the largest implications for moment coefficient, where the 26' wide decks had higher moment coefficients than the 46' wide decks did for a given beam type.
- Effect of bridge height: The higher superstructures increased the drag and moment coefficients relative to lower-profile superstructures.
- Effect of beam types: Differences in shape of drag, lift and moment coefficient were observed behavior between the I-girders and slab/box beams – where the girders had a falling and rising drag coefficient pattern while the box and slab beams had a simple increasing drag coefficient pattern. This observation strongly indicates that the spacing between I-girders

allows for more complex hydrodynamics to come into effect than the essentially monolithic closely-spaced slab.

6.3 Recommendation for Future Work

Plans for future work may include further investigation into bridge superstructures' hydrodynamics near the 0.8 and 1.0 inundation ratios, when the drag and lift coefficients drop, then begin their rise – trying to better model and understand the behavior at this range seems like it might have important implications on superstructure design. To better visualize this process and confirm that turbulent flow could be occurring over the top of the bridge deck, particle imaging velocimetry (PIV) could be utilized. Also, further study of hydrodynamic forces on scale models of a full-bridge structure, including abutments, pier foundation, pier cap and bearing, and bridge deck system, is recommended.

References

AASHTO. “AASHTO LRFD Bridge Design Specifications." *American Association of State Highway and Transportation Officials*, Washington, D.C. 2012

AASHTO, “Bridge Design Specifications.” *American Association of State Highway and Transportation Officials*, Washington, D.C., 2017. pp.4.

Arneson, L.A.,. “Evaluating Scour at Bridges (No. FHWA-HIF-12-003).” United States. *Federal Highway Administration*. 2013 pp 10.

Cigada, A., Malavasi, S. and Vanalil, M., “Direct Force Measurements on a Submerged Bridge Model.” *WIT Transactions on The Built Environment*, 2001. pp 56.

Chen, Q., Wang, L. and Zhao, H., “Hydrodynamic Investigation of Coastal Bridge Collapse during Hurricane Katrina.” *Journal of Hydraulic Engineering*, 2009. pp.175-186.

Diehl, Timothy H. Potential Drift Accumulation at Bridges" FHWA-RD-97-028, *Federal Highway Administration.* 1997. Table 2

FHWA (Federal Highway Administration),. “Bridges, Structures, and Hydraulics. 23 CFR 650”, 2009, subpart C.

Jempson, Mark “Flood and Debris Load on Bridges.” Doctorate Dissertation. The University of Queensland. 2000

Kara, S., Stoesser, T., Sturm, T.W. and Mulahasan, S., “Flow dynamics through a submerged bridge opening with overtopping.” *Journal of Hydraulic Research*, 2015. pp.186-195.

Kerenyi, K., Sofu, T., Guo, J., “Hydrodynamic forces on inundated bridge decks,” Rep. No. FHWAHRT-09-028. McLean, VA. 2009.

Lebbe, M.F.K., Lokuge, W., Setunge, S. and Zhang, K.,. “Failure mechanisms of bridge infrastructure in an extreme flood event.” *In Proceedings of the 1st International Conference on Infrastructure Failures and Consequences* (ICFC 2014) 2014. (pp. 124-132).

Malavasi, S. and Guadagnini, A., “Interactions between a rectangular cylinder and a free-surface flow.” *Journal of Fluids and Structures*, 2007. pp.1137-1148.

Naderi, N.,. “Numerical simulation of hydrodynamic forces on bridge decks”. (Master dissertation, TU Delft). 2018

Oudenbroek, K., Experimental research on hydrodynamic failure of river bridges on spread footings. (Master Thesis, TU Delft). 2018.

Oudenbroek, K., Naderi, N., Bricker, J.D., Yang, Y., Van der Veen, C., Uijttewaal, W., Moriguchi, S. and Jonkman, S.N., "Hydrodynamic and debris-damming failure of bridge decks and piers in steady flow". *Geosciences*, 8(11), 2018. p.409.

Hummel, M., Pervaiz, F. " Identify and Analyze Inundated Bridge Superstructures in High Velocity Flood Events -Task 3: Identifying Bridges with Potential Inundation in High Velocity Flow Events ." The University of Texas at Arlington, April 2020

Wardhana, K. and Hadipriono, F.C., "Analysis of recent bridge failures in the United States." *Journal of performance of constructed facilities*, 17(3) 2003., pp.144-150.

Appendix A

Sample calculations for TX-28 26-foot deck for inundation ratio, h*=1

Table A1: Bridge Dimensions (TX-28)

Attribute	**Actual Dimension (in)**	**Scale Dimension (in)**	**Scale Dimension (m)**
Deck thickness (s)	9.375	0.1875	0.0048
Bridge Length (L)	595	11.9	0.302
Width (W)	312	6.24	0.16
Girder Height	28	0.56	0.014
Railing height	32	0.64	0.016
Low Chord Elevation (h_b)	312	6.24	0.16
Superstructure Height, S (in)	69.875	1.3875	0.035

Table A2: Flow Data

Attribute	**Value**
Discharge (CFS)	0.575
Upstream water depth (in)	7.63
Average velocity (m/s)	0.276
Froude Number	0.20

Table A3: Supporting plate dimensions and lever arm

Attribute	**Value (in)**	**Value (m)**
Vertical plate height	5.5	0.1397
Plate thickness	0.1875	0.005
Length of the plate	3	0.076
Lever arm	9.7	0.246

Example calculation for a fully submerged bridge, h*=1.

*Note-while these calculations are performed for a 4-girder design not used in the experiment, the process and equations are identical to experimental procedure.

Inundation ratio,

$$h^* = \frac{(h_u - h_b)}{s} \quad \text{(A1)}$$

$$h^* = \frac{(0.194(m) - 0.159(m))}{0.035\ (m)}$$

$$h^* = 1$$

Where, h_u = upstream water depth, h_b =bridge low chord elevation, s = superstructure height

Submerged Area of the Bridge (in2)- for buoyant force,

$$A_{ss} = 4 * A_g + A_d + 2 * A_r 3 \quad \text{(A2)}$$

$$A_{ss} = 4 * 1.51e^{-4}(m^2) + 7.55e^{-4}(m^2) + 2 * 9.15e^{-5}(m^2)$$

$$A_{ss} = 1.54e^{-3}(m^2)$$

Where A_g= submerged girder area, A_d= submerged deck area, A_r= submerged railing area, as seen in Figure A1.

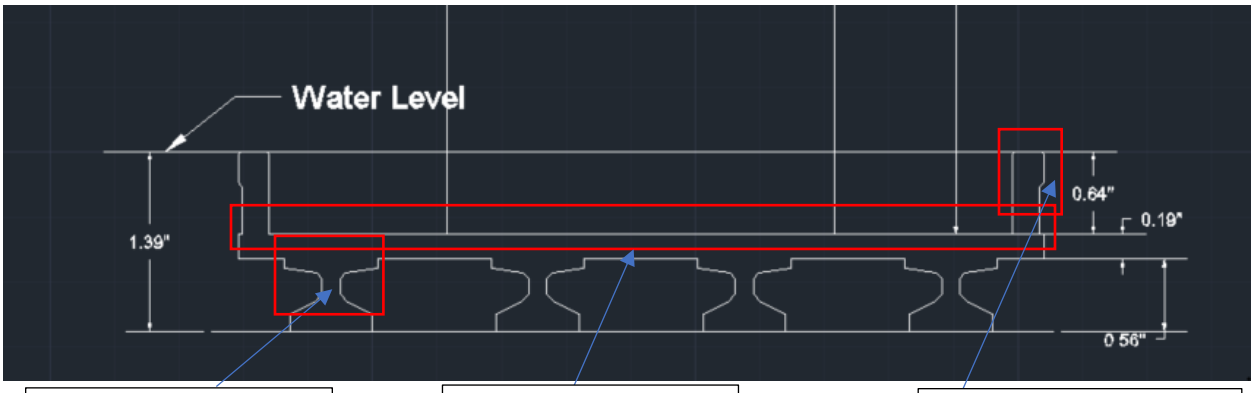

Figure A1- Submerged area definitions

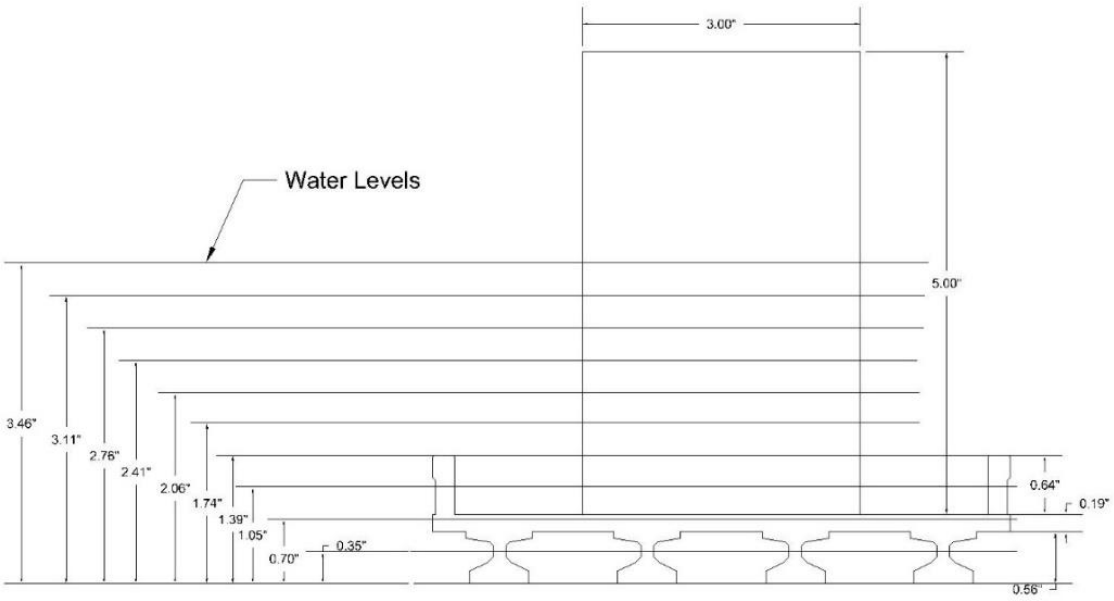

Figure A2- roadway deck & TX28 Superstructures at different Submergence Levels

Projected wetted area of the vertical plate (in2) normal to flow (For buoyancy and plate drag)

For h*=1, the height of the submerged plate normal to flow (Figure A2) =0.016 m

$$A_V = 2 * H_{SP} * T_{SP}\mathrm{t} \quad \text{(A3)}$$

$$A_V = 2 * 0.16(m) * 0.005(m)$$

$$A_V = 1.55e^{-4}\ (m^2)$$

where H_{SP}=height of submerged plate normal to flow, T_{SP}= thickness of submerged plate

Buoyant Force-F_B (N)

Volume of the Submerged Superstructure, V_{ss} (in3)

$$\mathrm{V_{ss}}=\mathrm{A_{ss}} * \mathrm{L} \quad \text{(A4)}$$

$$\mathrm{V_{ss}} = 1.54e^{-3}(m^2) * 0.032(m)$$

$$\mathrm{V_{ss}} = 4.6e^{-4}(m^3)$$

Volume of the submerged vertical plate $\mathrm{V_{sp}}$ (in3)

$$\mathrm{V_{sp}}=\mathrm{A_V} * L_{PFD} \quad \text{(A5)}$$

$V_{sp}=1.55e^{-4}(m^2)*0.076(\mathrm{m})$

$V_{sp}=1.2e^{-5}(m^3)$

Buoyant force at submergence h*=1,

$$F_B=\rho*g*(V_{SS}+V_{SP}) \quad \text{(A6)}$$

$$F_B=1000\left(\frac{\mathrm{kg}}{m^3}\right)*9.81\left(\frac{\mathrm{m}}{s^2}\right)*(4.6e^{-4}(m^3)+1.2e^{-5}(m^3))$$

$$F_B=4.69\ (\mathrm{N})$$

Where V_{SS}= volume of submerged superstructure, A_{SS}=area of submerged superstructure, L=bridge length, L_{PFD}= length of plate in flow direction, V_{SP}= volume of submerged vertical plate, F_B= buoyant force

Hydrostatic force-F_h (N)

For TX-28 narrow deck experiments, the upstream and downstream railing were both submerged under the water for inundation ratio, h*=1.00. (Figure A3) Based on this observation, hydrostatic force will be calculated for inundation ratio *0.25<h*<1.00* and for the respective part of the submerged upstream railing. Therefore, in this experiment, the hydrostatic is calculated for h*=0.75 as a sample.

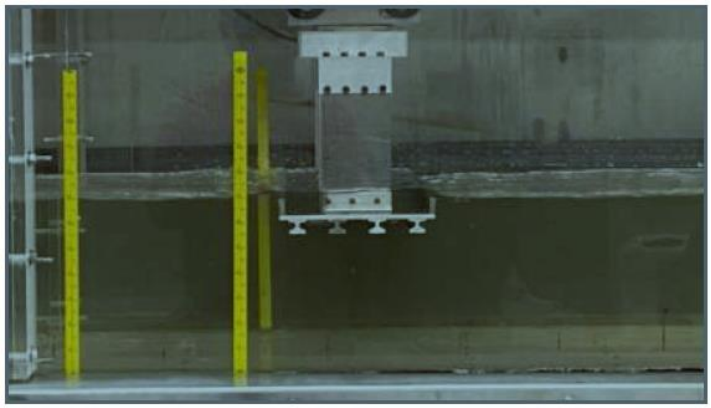

Figure A3- TX-28 bridge deck at h*=1

F_{h1}=hydrostatic force on the upstream side of the railing, (N)

h_{c1}=vertical distance from the water surface to the centroid of the area, (m)

h_1=upstream submerged superstructure depth (m)

$$h_1 = h_u - h_b \quad \text{(A7)}$$

$$h_1 = 0.194(m) - 0.167(m)$$

$$h_1 = 0.027\ (m)$$

$$h_b = 0.167\ m\ at\ h^* = 0.75$$

The total hydrostatic component of force on the upstream can be calculated as:

$$F_{h1} = \gamma h_{c1} A_{h1} \quad \text{(A8)}$$

$$F_{h1} = \frac{\gamma h_1}{2} h_1 * L$$

$$F_{h1} = \frac{9810 * 0.027^2 * 0.302}{2}$$

F_{h1}=1.04 (N)

The total hydrostatic component of force on the downstream can be calculated as:

$$F_{h2} = \gamma h_{c2} A_{h2} \quad \text{(A9)}$$

$$F_{h2} = \frac{\gamma h_2}{2} h_2 * L$$

$$F_{h2} = \frac{9810 * 0.026^2 * 0.302}{2}$$

$$F_{h2} = 0.97N$$

where

h_{c2} = Vertical distance from the water surface to the centroid of the area A_{h2} (m)

A_{h2} = projected area of the submerged superstructure on the downstream side (m^2)

h_d is downstream water level determined from observation, h_d=0.193 (m)

h_2 = downstream submerged superstructure depth (m)

$$h_2 = h_d - h_b \quad \text{(A10)}$$

$$h_2 = 0.193 - 0.167$$

$$h_2 = 0.026 \text{ m}$$

Viscous drag of the vertical plate (Jempson, 2000)

$$F_{DV} = 2.656 d_p \rho \sqrt{V^3 \vartheta l} \quad \text{(A11)}$$

F_{DV}=2.656*0.016*1000$\sqrt{0.276^3 * 1.05 * 10^{-6} * 0.076}$

$$F_{DV} = 1.77e^{-3}(N)$$

where

$$\mathrm{d_p} = \text{depth of the wetted } plate \text{ (in)}$$

$$d_p = \mathrm{h_u} - \mathrm{h_b} - \mathrm{G}_H - D_T \quad \text{(A12)}$$

$$d_p = 0.194(m) - 0.159(\mathrm{m}) - 0.014)\mathrm{m}) - 0.005(\mathrm{m})$$

$$d_p = 0.016\ (m)$$

G_H=girder height (m), D_T=deck thickness (m), ϑ = the kinematic viscosity (m^2/s), l = length of the plate in the direction of the flow (m), V= free stream velocity (m/s)

Pressure Drag on the vertical plate (Jempson, 2000)

$$F_{DP} = 0.5\ C_p \rho V^2 A_v \quad \text{(A13)}$$

$$F_{DP} = 0.5 * 1 * 1000 * 0.276^2 * 1.55e^{-4}$$

$$F_{DP} = 0.006\ (N)$$

where Cp=1 (considering that the pressure drag on the plates was typically 1% of the measured drag force), A_v= Projected wetted area of the submerged vertical plate (m^2), V= free stream velocity (m/s)

Drag Force-F_D

$$F_D = F_X - F_{DV} - F_{DP} - (F_{h1} - F_{h2}) \quad \text{(A14)}$$

$$F_D = 0.86 - 0.002 - 0.006 - 0$$

$$F_D = 0.85\ (N)$$

where $\mathrm{F_x}$ = Force in flow direction readout by the load cell (N) ,$\mathrm{F_{DV}}$ =, Viscous drag force due to vertical plates' hold on the bridge (N) $\mathrm{F_{DP}}$ = Pressure drag on the vertical plate (N), $\mathrm{F_{h1}}$ = hydrostatic force on the upstream bridge (N), $\mathrm{F_{h2}}$ = hydrostatic force on the upstream bridge (N)

Drag Coefficient (C_D)

$$C_D = \frac{2*F_D}{\rho V^2 A} \quad \text{(A15)}$$

$$C_D = \frac{2*0.85}{1000*0.276^2*(0.194-0.159)*0.302}$$

$$C_D = 2.10$$

Where $F_D = drag\ force\ (N)$, A= projected area on the bridge superstructure normal to flow direction (m^2), V= average stream velocity (m/s)

Lift Force $-F_L$ (N)-assuming horizontal water level

$$F_L = F_y - F_B \quad \text{(A16)}$$

$$F_L = 1.53 - 4.69$$

$$F_L = -3.16\ (\text{N})$$

Where F_L = Lift force(N) (positive upwards), F_y = Vertical force readout by the loadcell (N), F_B = Buoyant Force (N)

Lift Coefficient (CL)

$$C_L = \frac{2*F_L}{\rho V^2 A} \quad \text{(A17)}$$

$$C_L = \frac{2*(-3.16)}{1000*0.276^2*0.159*0.302}$$

$$C_L = -1.73$$

Where A= cross sectional- area on the bridge superstructure (m^2) (along the flow direction),

V= average stream velocity (m/s)

Corrected Moment-M_{corr} (NM)

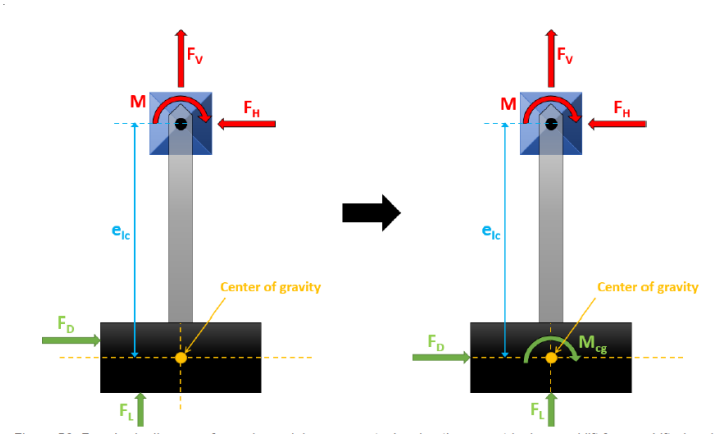

Figure A4- Free-body diagram of the scale model showing the eccentric drag and lift force shifted under addition of moment, M_{cg}, the moment acting on a component, measured around the center of gravity (positive clockwise) – Figure A4.

$$M_{cg} = M - F_D * e_{lc} \quad \text{(A18)}$$

$$M_{cg} = -0.23 - 0.85 * 0.246$$

M_{cg} =-0.44 (NM) (positive in clockwise)

Where $M = \text{moment readout by loadcell (NM)}$, $F_D = \text{drag force (N)}$, e_{lc}=Moment arm between the center of gravity of the components and the center of the load cell (m).

To find e_{lc}, the distance from the centroid of the instrument to the girder soffit (in) = 10.25=0.260 m. Centroid of the superstructure from girder soffit (in) = 0.5494=0.014 m.

$$e_{lc} = 0.260 - 0.014 = 0.246\, m$$

Moment Coefficient (CM)

$$C_M = \frac{2*M_{cg}}{\rho V^2 L W^2} \quad \text{(A19)}$$

$$C_M = \frac{2*0.44}{1000*0.276^2*0.302*0.159^2}$$

$$C_M = 1.54$$

Where L= length of the bridge deck (m), W=width of the bridge deck (m), V= average stream velocity (m/s)